


Article

Petrogenesis and Tectonic Significance of Early Permian Intermediate–Felsic Rocks in the Southern Beishan Orogen, Northwest China: Geochronological and Geochemical Constraints

Runwu Li ^{1,2}, Shangguo Su ^{1,*} , Huiyi Sun ², Ruibin Liu ² and Yutian Xia ²

¹ School of Earth Sciences and Resources, China University of Geosciences, Beijing 100010, China; lirw1995@163.com

² Beijing SHRIMP Center, Institute of Geology, Chinese Academy of Geological Sciences, Beijing 100010, China; sunhuiyi@bjshrmp.cn (H.S.); 1901111999@pku.edu.cn (R.L.); xiayt1997@163.com (Y.X.)

* Correspondence: susg@cugb.edu.cn

Abstract: Permian intermediate–felsic igneous rocks, widely distributed in the southern Beishan orogen, provide crucial constraints on the geodynamic process of the late Paleozoic Paleo-Asian Ocean. New zircon U–Pb dating using LA–ICP–MS determines the age of the northern Qingshan diorites, the Heishantou quartz diorites, and the southern Qingshan biotite granodiorites at 300 Ma, 294 Ma, and 291–286 Ma, respectively. Their whole-rock compositions exhibit arc-like geochemical features. Moreover, their zircon trace elements show the characteristics of continental arc zircons. The diorites, characterized by low SiO₂, high MgO with Mg# (50–52), and low Cr, Co, and Ni, display enrichment in Sr–Nd–Hf isotopes (⁸⁷Sr/⁸⁶Sr = 0.7060 to 0.7061; ε_{Nd}(t) = –1.4 to –1.7; ε_{Hf}(t) = –4.7 to –0.6), originating from the fractionation process of magma derived from the enriched mantle. The quartz diorites show moderate SiO₂ and variable MgO (2.75–3.84 wt%) and exhibit enrichment in Sr–Nd (⁸⁷Sr/⁸⁶Sr = 0.7048–0.7050; ε_{Nd}(t) = –1.5–+0.9) and depletion in zircon Hf isotopes (ε_{Hf}(t) = 3.8 to 7.8). Combined with their high Y (20.0–21.0 ppm) and low (La/Yb)_N (6.0 to 17.2), we conclude that they originated from the juvenile lower crust previously influenced by oceanic sediments, with the input of enriched mantle-derived materials. The biotite granodiorites display low A/CNK (0.91–0.97), 10000*Ga/Al (1.8–1.9), and Ti-in-zircon temperatures (average 711 °C), indicating that they are I-type granitoids. These rocks show enrichment in Sr–Nd isotopes (⁸⁷Sr/⁸⁶Sr = 0.7054 to 0.7061; ε_{Nd}(t) = –2.0 to –1.6) and many variable zircon Hf isotopes (ε_{Hf}(t) = –2.3 to +4.5). Geochemical studies indicate that they originate from the mixing of magmas derived from the enriched mantle and preexisting juvenile lower crust. All these data imply the existence of oceanic subduction in southern Beishan during the early Permian. Integrating these results with previous studies, it is inferred that the retreating subduction of the Liuyuan Ocean contributed to early Permian intermediate–felsic rocks becoming widespread in the Shibanshan unit, the southernmost part of the Beishan orogen, and also why the Paleo-Asian Ocean in southern Beishan did not close during the early Permian.

Keywords: early Permian; magmatism; retreating subduction; Beishan; central Asian orogenic belt



Citation: Li, R.; Su, S.; Sun, H.; Liu, R.; Xia, Y. Petrogenesis and Tectonic Significance of Early Permian Intermediate–Felsic Rocks in the Southern Beishan Orogen, Northwest China: Geochronological and Geochemical Constraints. *Minerals* **2024**, *14*, 114. <https://doi.org/10.3390/min14010114>

Academic Editors: Fuhao Xiong, Bin Liu and Aleksei V. Travin

Received: 5 December 2023

Revised: 18 January 2024

Accepted: 19 January 2024

Published: 22 January 2024



Copyright: © 2024 by the authors. Licensee MDPI, Basel, Switzerland. This article is an open access article distributed under the terms and conditions of the Creative Commons Attribution (CC BY) license (<https://creativecommons.org/licenses/by/4.0/>).

1. Introduction

The Central Asian Orogenic Belt (CAOB), one of the largest accretionary orogenic belts in the world, is situated along the Siberian Craton and the North China and Tarim Cratons (Figure 1(1)). The CAOB formed through multi-stage accretionary-collisional processes of the Paleo-Asian Ocean (PAO) during the Neoproterozoic and Phanerozoic periods and consists primarily of microcontinental blocks, ophiolites, sea mountains, subduction–accretion complexes, magmatic arcs, and related basins [1–3]. Recently, the Nd isotope mapping results of intermediate–felsic magmatic rocks in the CAOB revealed that the areal

proportion of the juvenile crust is approximately 58% [4], supporting substantial continental growth within the CAO. Moreover, the CAO hosts a diverse range of world-class ore deposits, including porphyry Cu–(Au)–(Mo) deposits and numerous other polymetallic magmatic–hydrothermal deposits, showing significant mineral resource potential. The comprehension of the subduction–accretion history of the PAO is crucial for revealing the continental growth mechanisms and metallogenic significance of the CAO [5–7].

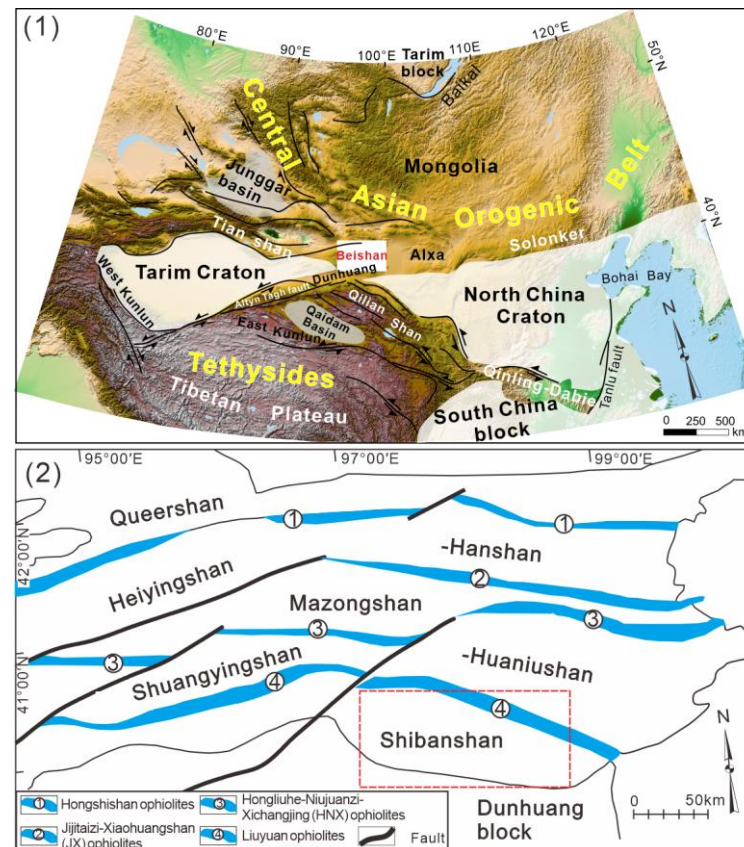


Figure 1. (1) Simplified tectonic map showing the CAO, Tethysides, and Tarim and North China Cratons (modified after [1]); (2) Tectonic map of the Beishan orogen (modified after [8]).

The Beishan orogen, linking the Southern Tian Shan suture and the Solonker suture, occupies a vital region of the central part of the southern CAO (Figure 1(1)) [8]. Moreover, it acts as a crucial junction point connecting the CAO and Tethys orogenic belt (Figure 1(1)) [9,10]. The Beishan orogen thus offers an ideal place for investigating the geodynamic interactions between these two orogenic belts. Regarding the geodynamic evolution of this orogen during the Paleozoic, many works have focused on intrusive rocks, volcanic–sedimentary rocks, and structural geology, and much progress has been achieved [11–16]. For instance, several ophiolitic mélanges and regional faults have been recognized in the Beishan region (Figure 1(2)) [8]. They likely represent the different branches of the PAO and segment the Beishan orogen into different tectonic units (Figure 1(2)) [11,12]. It is generally accepted that the early Paleozoic magmatism, which is widespread in the different units of the Beishan orogen, forms in an arc-related setting [12,14]. However, the late Paleozoic geodynamic process and the timing of the termination of the Beishan orogen are controversial. In particular, the Permian tectonic setting in this orogen remains under debate. Different tectonic models, including a subduction-related arc setting [16,17], a mantle plume-related setting [18], and a post-collisional extensional setting [19,20], have been suggested. These controversies hamper our understanding of the evolutionary history of the PAO and the accretionary–collisional processes of the Beishan orogen. Permian magmatism, which is widely distributed in southern Beishan, offers a promising means to

resolve the above disputes. Variations in magmatic compositions can be formed either in an ideal closed magmatic system through the partial melting and fractionation processes of different source materials under various conditions [21,22] or in an open magmatic system through the mixing process between different magmas and the wall–rock assimilation–fractional crystallization process (AFC) [23,24]. Other magmatic processes, such as liquid immiscibility and vapor-phase leaching [25,26], are also proposed to explain magmatic compositional changes. However, no evidence suggests that they perform a crucial role in producing chemical variations in igneous rocks [27]. The compositional changes in natural igneous rocks can be influenced by multiple magmatic processes, with some being dominant while others are secondary [27,28]. Generally, rock associations and geochemical compositions of magmatic rocks reflect the characteristics of their magma sources and formation conditions [29,30], thus offering insights into geodynamic settings.

This study presents new LA–ICP–MS zircon U–Pb dating and trace elements, whole-rock geochemical data, and Sr–Nd–Hf isotopes for early Permian intermediate–felsic igneous rocks from southern Beishan (Figures 1(2) and 2). Combined with previous regional studies, our new data constrain the petrogenesis of these igneous rocks and provide a strong basis for understanding the early Permian geodynamic evolution in southern Beishan.

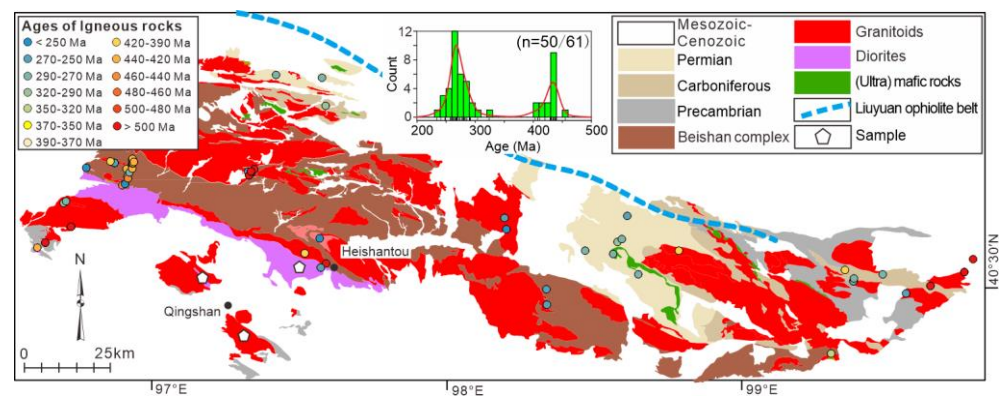


Figure 2. Geological map of the Shibanshan unit showing the sampling location in the Shibanshan unit. The ages of igneous rocks are presented in Supplementary Table S1. The inserted histogram shows the compiled zircon U–Pb ages in the study area. Only 51 of the total 62 age data are included.

2. Geological Background and Description of Samples

2.1. Geological Background

The Beishan orogen extends across the Xinjiang–Gansu Inner Mongolia region, connecting the Dunhuang block and the Alxa block (Figure 1(1)). It is divided into five tectonic units by four east–west-oriented ophiolitic mélangé belts (Figure 1(2)) [8]. The Shibanshan unit, the southernmost tectonic unit, is situated to the south of the Liuyuan mélangé belt and to the north of the Dunhuang block (Figure 1(2)). The Liuyuan mélangé belt intermittently stretches for about 300 km along both sides of the Liuyuan–Daqishan–Zhangfangshan fault and is mainly exposed in the regions of Huitongshan, Liuyuan, and Zhangfangshan (Figure 1(2)) [31,32]. Notably, the Liuyuan complex has been extensively studied [17,33,34]. Zircon U–Pb dating results for the Liuyuan ophiolitic mélangé belt span from 504 to 270 Ma [33–35]. Moreover, geochemical analyses indicate that the basalts and gabbros from this ophiolitic mélangé belt exhibit signatures typical of mid-ocean ridge basalt (MORB) and island arc basalt (IAB) [17,34]. Previous works argue that the Liuyuan complex was likely generated in a fore-arc setting [17] or a back-arc basin [34].

The Shibanshan unit is predominantly composed of the Beishan complex, upper Paleozoic, and Paleozoic intermediate–felsic intrusive rocks (Figure 2) [8]. The Beishan complex mainly consists of felsic gneiss, biotite–plagioclase gneiss, and metamorphic sedimentary rocks [36]. The origins and tectonic implications of the Beishan complex remain controversial. Some propose that the Beishan complex developed in an arc setting during the Paleozoic [36]. However, other studies argue that it represents the Precambrian

microcontinent in southern Beishan [37,38]. The strata of the Carboniferous–Permian are widely distributed (Figure 2). The Carboniferous strata primarily consist of clastic rocks, slates, phyllites, limestones, and intermediate–felsic volcanic rocks. The Permian strata are mainly composed of clastic sedimentary rocks, pyroclastic rocks, and mafic–intermediate and felsic volcanic rocks [8,20]. Paleozoic magmatism, dominantly intermediate–felsic intrusive rock, is widespread in the Shibanshan unit, mainly as Carboniferous–Permian granitoids and minor diorites (Figure 2 and Table S1). These rocks show different mineral assemblages and geochemical and Sr–Nd–Hf isotope compositions, which likely record the history of the geodynamic evolution in southern Beishan during the Paleozoic [12,16].

2.2. Description of Samples

In this study, we investigated three intermediate–felsic intrusive plutons, including the Heishankou, southern Qingshan, and northern Qingshan plutons (Figure 2), in the Shibanshan unit. The northern Qingshan pluton is composed of early granitoids and later intruding diorites (Figure 3(1)). The early granitoids, covering an area of about 150 km², intrude into the Precambrian strata (Figure 2). The diorites, forming as a stock, show an exposed area of approximately 6 km² (Figure 2). The diorites sampled in this study are dark gray and medium-grained (Figure 3(1)), primarily consisting of plagioclases (50 vol%), quartzes (5–10 vol%), amphiboles (35–40 vol%), and biotites (~5 vol%). Euhedral to subhedral plagioclases present a zoning texture and polysynthetic twinning (Figure 3(4)). Their interiors generally show a slight alteration, appearing blurred compared to their edges (Figure 3(4)). Dark green amphiboles are anhedral, whereas biotites are subhedral to euhedral. Quartzes are anhedral as interstitial crystals (Figure 3(4)). Furthermore, the presence of amphiboles with residual pyroxene (Figure 3(4)) implies that the preexisting pyroxene reacted with the surrounding magma [39]. Three rock samples were collected from the diorite pluton. All were determined for whole-rock major and trace element contents; one sample was selected for the analyses of zircon U–Pb dating and Lu–Hf isotopes, and two rocks were used for the whole-rock Sr–Nd isotope measurement.

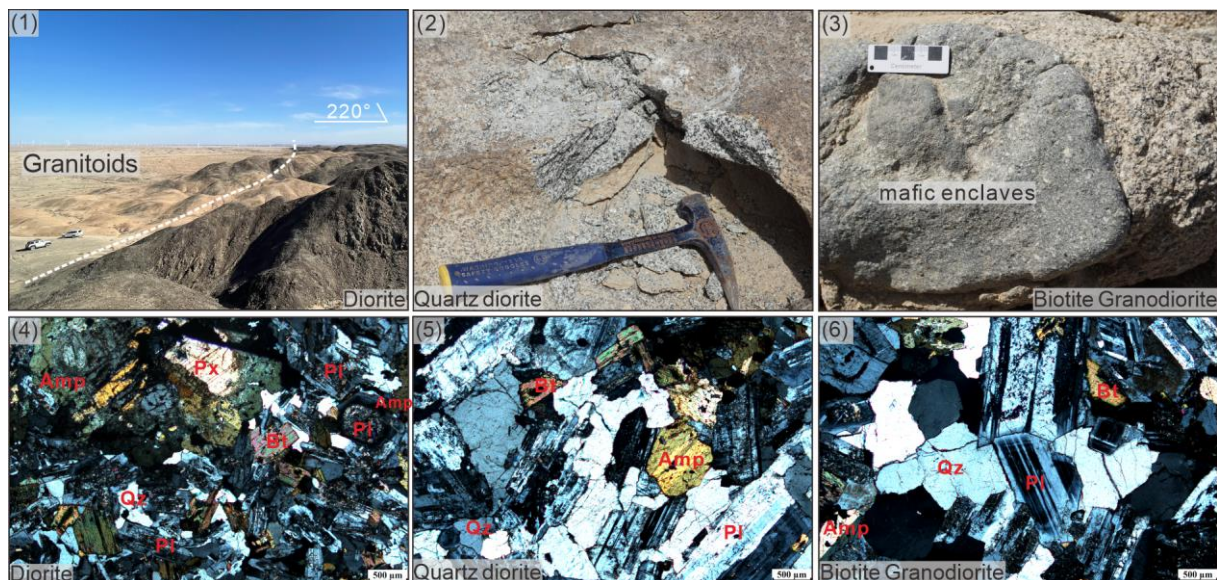


Figure 3. Representative field images and photomicrographs of the sampled rocks in the Shibanshan unit. (1,4) The northern Qingshan diorite; (2,5) The Heishankou quartz diorite; (3,6) The southern Qingshan biotite granodiorite. Abbreviations: Px—pyroxene; Amp—amphibole; Pl—plagioclase; Bt—biotite; Qz—quartz.

The Heishankou pluton extends nearly east–west for approximately 90 km and covers an area of approximately 350 km² (Figure 2). Here, we focused on the eastern section of this pluton, which consists mainly of the quartz diorites sampled in this study and minor

granodiorites with less mafic minerals (amphibole and biotite). The quartz diorites are light gray and medium-grained (Figure 3(2)) and are mainly composed of plagioclases (~60 vol%), quartzes (15 vol%), amphiboles (10–15 vol%), biotites (10 vol%), as well as minor K-feldspars (~1 vol%) (Figure 3(5)). Plagioclases are euhedral to subhedral, generally displaying polysynthetic twinning, with some Carlsbad–albite twins observed (Figure 3(5)). Greenish-brown amphiboles are subhedral to anhedral, while biotites appear subhedral as interstitial minerals (Figure 3(5)). Four rocks were collected from the quartz diorite pluton. All rock samples were measured for whole-rock major and trace element compositions, with one rock chosen for the measurement of zircon U–Pb dating and Lu–Hf isotopes and two rocks selected for the determination of whole-rock Sr–Nd isotopes.

The southern Qingshan pluton, occupying an area of about 100 km² (Figure 2), intrudes into the Precambrian strata (Figure 2) and is primarily composed of the biotite granodiorites collected in this study and diorites (Figure 3(3)). Moreover, abundant mafic enclaves have developed in the southern Qingshan pluton (Figure 3(3)). The biotite granodiorites are light gray and medium-grained and consist of plagioclases (40–45 vol%), K-feldspars (~5 vol%), quartzes (30–35 vol%), amphiboles (~10 vol%), and biotites (~5 vol%) (Figure 3(6)). Euhedral to subhedral plagioclases commonly show polysynthetic twinning, with some interiors exhibiting a slight alteration (Figure 3(6)). Minor K-feldspars with Carlsbad twins are observed. Dark green amphiboles and brown biotites are subhedral to anhedral as interstitial minerals (Figure 3(6)). Eight rocks were collected from this pluton. All rocks underwent analyses for whole-rock major and trace element compositions, with two rocks selected for zircon U–Pb dating and Lu–Hf isotopes, and three rocks chosen for whole-rock Sr–Nd isotope analyses.

3. Analytical Methods

3.1. Zircon U–Pb and Lu–Hf Isotopic Analyses

Conventional heavy liquid and magnetic techniques were employed to extract zircons. Subsequently, these grains were mounted in epoxy resin and polished to roughly half-thickness at the Shougang Geological Exploration Institute, China. Grains showing euhedral to subhedral shapes, distinct zoning textures, and no fractures and inclusions under cathodoluminescence (CL), transmission, and reflection images were selected as potential zircon specimens for U–Pb dating and Lu–Hf isotopes.

Zircon U–Pb dating was performed using laser ablation (LA)–ICP–MS in the Mineral and Fluid Inclusion Microanalysis lab, Institute of Geology, Chinese Academy of Geological Sciences, Beijing, China. Zircon 91500 and SA01 were analyzed twice and once, respectively, for every 12 sample points analyzed. Detailed analytical methods are described in [40,41]. The Iolite software (ver. 3.7) was used for the reduction in analyzed data [42]. The exponential function was used to calibrate the downhole fractionation [42]. No corrections for common lead were implemented, and the reported errors in Table S2 represent 2 sigma values. NIST610 and 91Zr served as external and internal standards for calibrating the zircon trace element contents, respectively. Concordia diagrams and weighted mean calculations of U–Pb age were constructed using Isoplot (ver. 3.0) [43].

The determination of in situ zircon Lu–Hf isotopes was completed using a Resolution S155 laser ablation microprobe attached to a Neptune multicollector ICP–MS (LA-MC-ICP–MS) at the MNR Key Laboratory of Metallogeny and Mineral Assessment, Institute of Mineral Resources, Chinese Academy of Geological Sciences, Beijing. The instrumental conditions and data collection were thoroughly described by [44,45]. The reference standard during our measurement was zircon GJ-1. Analytical data were processed offline (including sample and blank signal selection and mass bias calibrations) using the software ICPMSDataCal (ver. 11.4). The $\epsilon_{\text{Hf}}(t)$ values and Hf model ages ($T_{\text{DM}}^{\text{Hf}}$) were calculated using the ^{176}Lu – ^{177}Hf decay constant of $1.867 \times 10^{-11} \text{ yr}^{-1}$ [46], chondrite ratios of $^{176}\text{Hf}/^{177}\text{Hf} = 0.282772$ and $^{176}\text{Lu}/^{177}\text{Hf} = 0.0332$ [47], and DM parameters of $^{176}\text{Hf}/^{177}\text{Hf} = 0.28325$ and $^{176}\text{Lu}/^{177}\text{Hf} = 0.0384$ [48].

3.2. Whole-Rock Major and Trace Elements

The measurement of whole-rock major and trace elements was carried out at the Wuhan SampleSolution Analytical Technology Co., Ltd., Wuhan, China. The sample pre-treatment for the analysis of whole-rock major elements was made using the melting method. The flux is a mixture of $\text{Li}_2\text{B}_4\text{O}_7$, LiBO_2 , and LiF (45:10:5). NH_4NO_3 and LiBr were employed as oxidant and release agents, respectively. The melting temperature was 1050 °C, and the melting time was 15 min. Zsx Primus II wavelength dispersive X-ray fluorescence spectrometer (XRF) produced by RIGAKU, Japan, was adopted for the determination of whole-rock major elements. The relative standard deviation (RSD) was less than 2%. The measurement of whole-rock trace elements was performed on an Agilent 7700e ICP-MS, and the analytical precision was better than 10%. The standards BHVO-2, BCR-2, RGM-1, and JA-2 were used to monitor the data quality. Detailed sample preparation methods, as well as analytical precision and accuracy for the analysis of whole-rock trace elements, are described in [49].

3.3. Whole-Rock Sr-Nd Isotopic Analyses

Sr-Nd isotopes and Rb, Sr, Sm, and Nd concentrations for the Heishantou quartz diorites and southern Qingshan biotite granodiorites were completed at the Institute of Precambrian Geology and Geochronology, Russian Academy of Sciences. The Sr-Nd isotopes were analyzed using a Triton TI (Finnigan MAT, Bremen, Germany) multicollector solid-phase mass spectrometer in the static mode. The method of isotopic dilution was used to determine the concentrations of Rb, Sr, Sm, and Nd trace elements. Detailed processes are similar to those described in [50]. The $^{87}\text{Sr}/^{86}\text{Sr}$ and $^{143}\text{Nd}/^{144}\text{Nd}$ ratios were normalized to 0.1194 and 0.7219, respectively. During data collection, repeated measurements of the NBS987 and JNdi-1 standard solutions provided average values for $^{87}\text{Sr}/^{86}\text{Sr}$ and $^{143}\text{Nd}/^{144}\text{Nd}$, at 0.710262 ± 0.000005 (2σ , $n = 6$) and 0.512103 ± 0.000003 (2σ , $n = 5$), respectively. Sr-Nd isotope analyses for the northern Qingshan diorites were carried out at the University of Science and Technology of China, Hefei, China. The Sr-Nd isotopes were analyzed using a Finnigan MAT 262 mass spectrometer. The $^{87}\text{Sr}/^{86}\text{Sr}$ and $^{143}\text{Nd}/^{144}\text{Nd}$ ratios were normalized to 0.1194 and 0.7219, respectively. Detailed analysis processes were similar to those described in [51,52]. During data collection, repeated measurements of the NBS987 and JNdi-1 standard solutions provided average values for $^{87}\text{Sr}/^{86}\text{Sr}$ and $^{143}\text{Nd}/^{144}\text{Nd}$ at 0.710245 ± 0.000012 (2σ , $n = 3$) and 0.512116 ± 0.000008 (2σ , $n = 3$), respectively. The values of $(^{147}\text{Sm}/^{144}\text{Nd})_{\text{CHUR}}$ (0.1967), $(^{143}\text{Nd}/^{144}\text{Nd})_{\text{CHUR}}$ (0.512638), $(^{147}\text{Sm}/^{144}\text{Nd})_{\text{DM}}$ (0.2136), and $(^{147}\text{Nd}/^{144}\text{Nd})_{\text{DM}}$ (0.513151) were employed to calculate all the $\epsilon_{\text{Nd}}(t)$ values and model ages in this study [53,54].

4. Analytical Results

4.1. Zircon U-Pb Ages and Lu-Hf Isotope Compositions

Zircon U-Pb dating and Lu-Hf isotope results are shown in Supplementary Tables S2 and S3, respectively. Zircons from the four rock samples in the Shibanshan unit generally appear light to dark gray in the cathodoluminescence (CL) images (Figure 4). These zircon grains typically exhibit euhedral to subhedral and prismatic shapes, with lengths varying from ~60 to 120 μm and widths from ~30 to 70 μm . Zircons from the northern Qingshan diorite (G22924-11.1) display relatively high aspect ratios of 2:1 to 5:1, while those from the other three samples (G22917-2.1, G22919-5.1, and G22923-2.1) have low aspect ratios of 2:1 to 3:1 (Figure 4). All analyzed zircon spots exhibit clear rhythmic zoning in the CL images (Figure 4). With the exception of one zircon from the biotite granodiorite (G22923-2) that shows a high, flat rare earth element (REE) pattern indicative of chemical alteration [55], all analyzed zircons demonstrate steeply rising REE distribution patterns from La to Lu and exhibit positive Ce and negative Eu anomalies (Figure S1), suggesting their magmatic origins [55,56]. Furthermore, in the $(\text{Sm}/\text{La})_{\text{N}}$ vs. La and Th vs. U diagrams (Figure 5), they are plotted within the magmatic zircon field, providing additional evidence for their igneous origins [57,58].



Figure 4. Cathodoluminescence (CL) images of the analyzed zircons. The red and yellow circles on zircons show the positions for U-Pb dating and Lu-Hf isotope analysis, respectively. The numbers below zircons represent $^{206}\text{Pb}/^{238}\text{U}$ ages and $\epsilon_{\text{Hf}}(t)$ values, respectively.

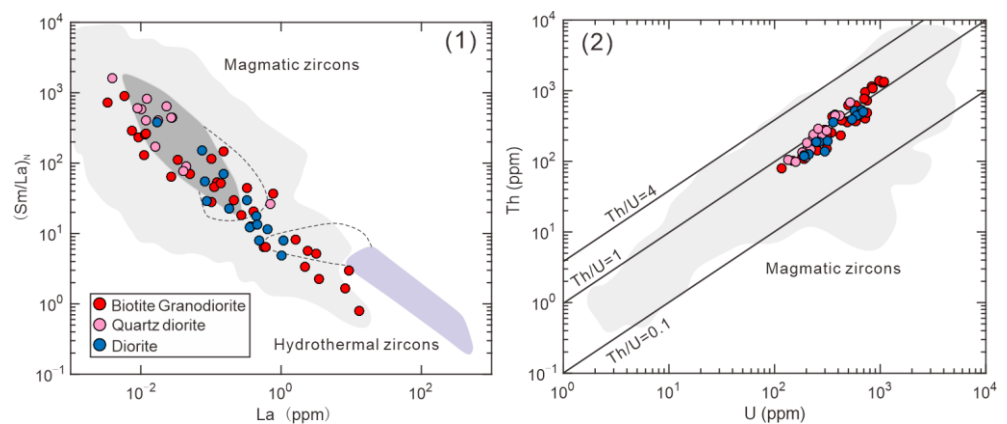


Figure 5. (1) $(\text{Sm}/\text{La})_{\text{N}}$ vs. La and (2) Th vs. U diagrams for the analyzed zircons. The notation “N” indicates chondrite-normalized values. The magmatic and hydrothermal zircon fields (dark gray and purple shaded areas, respectively) with extensions (dashed line) illustrated in (1) are from [55]. The broader magmatic zircon fields (light gray shaded area) in (1,2) are from [58].

Fourteen zircons from the northern Qingshan diorite (G22924-11.1) yielded $^{206}\text{Pb}/^{238}\text{U}$ ages of 310 to 291 Ma, with a weighted mean age of 300 ± 2 Ma ($n = 14$, MSWD = 1.2) (Figure 6(1)). Eleven zircons were chosen for the analysis of Lu-Hf isotopes. They exhibited $\epsilon_{\text{Hf}}(t)$ values ranging from -4.7 to -0.6 and relatively old two-stage Hf model aged (T_{DM2Hf}) between 1614 Ma and 1355 Ma.

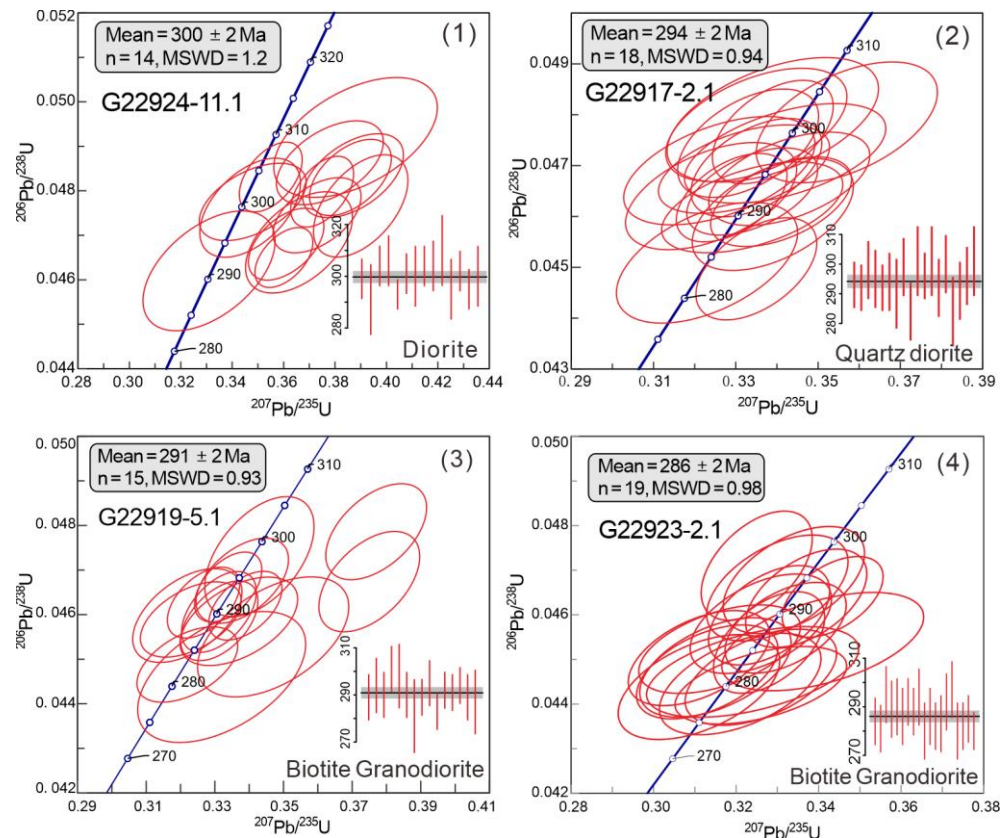


Figure 6. Concordia diagrams and weighted mean $^{206}\text{Pb}/^{238}\text{U}$ ages for the sampled rocks in the Shibanshan unit. (1) The northern Qingshan diorite; (2) The Heishankou quartz diorite; (3,4) The southern Qingshan biotite granodiorites.

Eighteen zircons from the Heishantou quartz diorite (G22917-2.1) yielded $^{206}\text{Pb}/^{238}\text{U}$ ages ranging from 301 to 284 Ma, with a weighted mean age of 294 ± 2 Ma ($n = 18$, MSWD = 0.94) (Figure 6(2)). Fifteen dated zircon grains were selected for the determination of Lu-Hf isotopes. Their $\epsilon_{\text{Hf}}(t)$ values varied from 3.8 to 7.8, with young T_{DM2Hf} between 1059 and 813 Ma.

Zircons of two biotite granodiorites from the southern Qingshan pluton were analyzed. Fifteen zircons from sample G22919-5.1 yielded $^{206}\text{Pb}/^{238}\text{U}$ ages ranging from 301 to 281 Ma, with a weighted mean age of 291 ± 2 Ma ($n = 15$, MSWD = 0.93) (Figure 6(3)). All fifteen zircons were analyzed for Lu-Hf isotopes. The $\epsilon_{\text{Hf}}(t)$ values vary from -2.3 to 4.5 with T_{DM2Hf} from 1453 to 1021 Ma. For sample G22923-2.1, twenty zircons were measured. One zircon (G22923-2-1-2) showed a strong influence on chemical alteration, as discussed above, and its age data were eliminated. Nineteen zircons generated $^{206}\text{Pb}/^{238}\text{U}$ ages ranging from 297 to 280 Ma, with a weighted mean age of 286 ± 2 Ma ($n = 19$, MSWD = 0.98) (Figure 6(4)). Additionally, fourteen zircon grains were analyzed for Lu-Hf isotope compositions. Their $\epsilon_{\text{Hf}}(t)$ values varied from -0.9 to 2.9 with T_{DM2Hf} from 1364 to 1113 Ma.

4.2. Whole-Rock Major and Trace Element Geochemistry

Whole-rock major and trace element compositions are shown in Supplementary Table S4. All analyzed rocks exhibited a low loss on ignition (LOI) content ranging from 0.58 to

1.37 wt%, indicating limited weathering and/or alteration. Major element contents in this study are normalized to 100 wt% on a volatile-free basis. The northern Qingshan diorites display low SiO₂ contents (54.68–55.25 wt%) and high Al₂O₃ (17.89–18.00 wt%), TFe₂O₃ (8.22–8.78 wt%), and MgO (4.46–4.53 wt%) contents with Mg# values (molar 100 × Mg/(Mg + Fe²⁺)) of 50 to 52 (Figures 7 and 8). Additionally, these rocks show moderate total alkali (Na₂O + K₂O) contents (Figure 7(1)). They are sodium-rich with low K₂O/Na₂O ratios (0.5–0.6), belonging to calc-alkaline series rocks in the SiO₂ vs. K₂O diagram (Figure 7(2)). The diorites display slight enrichment in light REEs (LREEs) relative to heavy REEs (HREEs) ((La/Yb)_N = 5.9–6.2) with no clear anomalies of Eu (Eu/Eu* = 0.9–1.0) (Figure 9(1)). Furthermore, these rocks exhibit positive anomalies in Rb, Th, U, K, and Pb and negative anomalies in Nb, Ta, and Ti (Figure 9(2)).

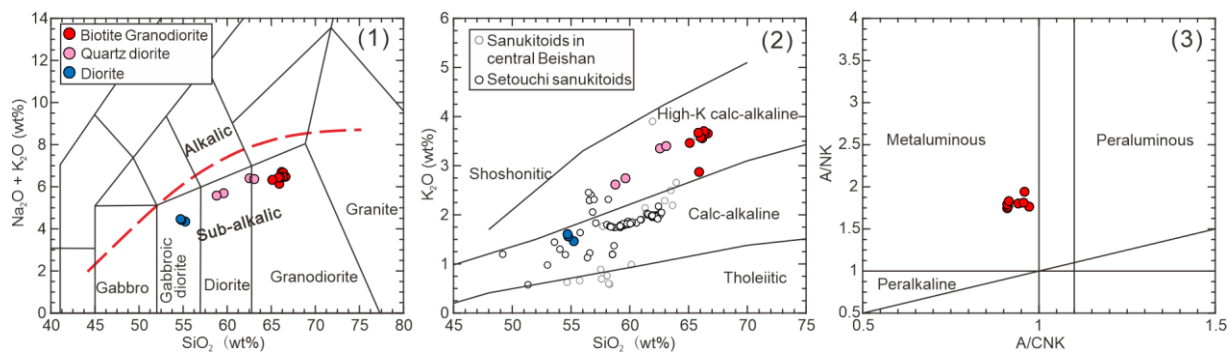


Figure 7. (1) Total alkali (Na₂O + K₂O) vs. SiO₂ diagram [59]; (2) K₂O vs. SiO₂ diagram [60]; (3) A/NK vs. A/CNK diagram [61]. A/NK = (mol) Al₂O₃/(Na₂O + K₂O) and A/CNK = (mol) Al₂O₃/(Na₂O + K₂O + CaO).

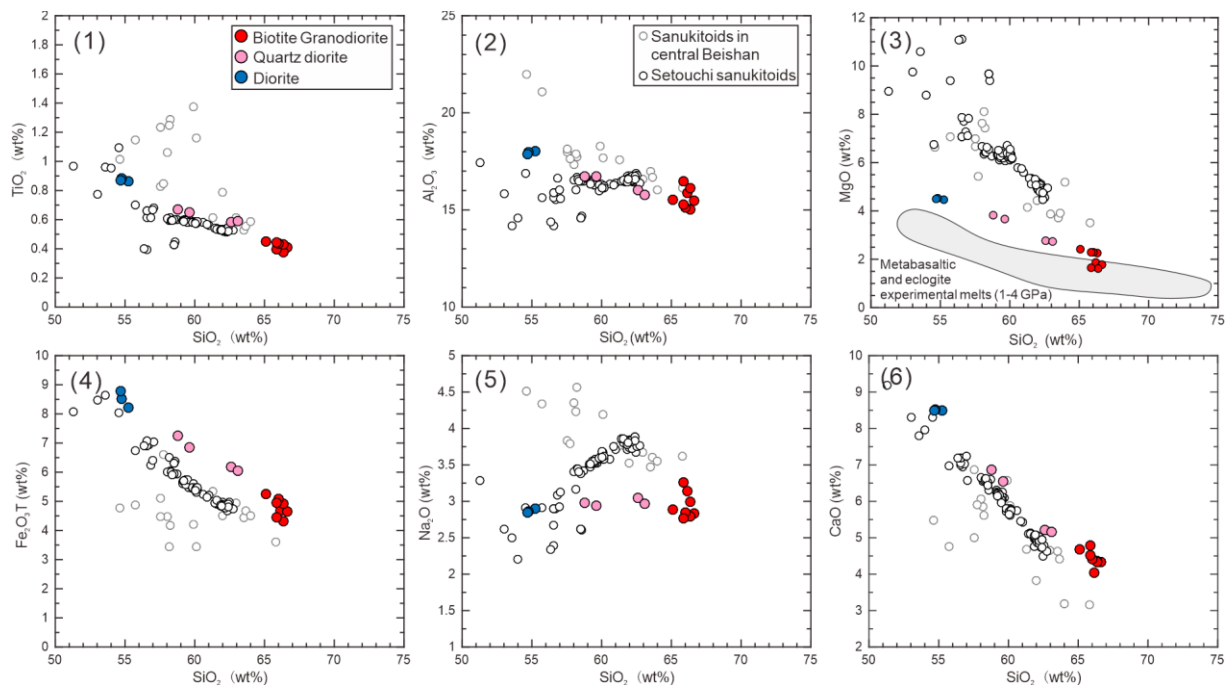


Figure 8. Diagrams of various major elements vs. SiO₂ contents. (1) TiO₂ vs. SiO₂; (2) Al₂O₃ vs. SiO₂; (3) MgO vs. SiO₂; (4) Fe₂O₃T vs. SiO₂; (5) Na₂O vs. SiO₂; (6) CaO vs. SiO₂. The Setouchi sanukitoid data are from [62–64]. The central Beishan sanukitoid data are from [13,65]. The data for metabasaltic and eclogite experimental melts (1–4.0 GPa) are from [66–70].

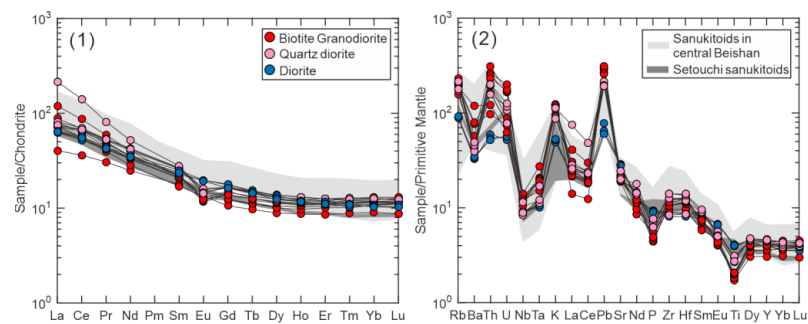


Figure 9. (1) Chondrite-normalized REE patterns; (2) Primitive-mantle-normalized trace element spiderdiagrams. Data for the Setouchi and central Beishan sanukitoids are from the same source as those in Figure 8. Data for the chondrite and primitive mantle are from [71].

Heishantou quartz diorites display moderate and variable SiO_2 contents (58.79–63.08 wt%) and a moderate total alkali, Al_2O_3 (15.76–16.72 wt%), TFe_2O_3 (6.05–7.24 wt%), and MgO (2.75–3.84 wt%) content with Mg# values of 47 to 52 (Figures 7 and 8). They show enrichment of K_2O with high $\text{K}_2\text{O}/\text{Na}_2\text{O}$ ratios (0.9–1.1), belonging to the high-K calc-alkaline series (Figure 7(2)). The quartz diorites show variable $(\text{La}/\text{Yb})_N$ ratios ranging from 6.0 to 17.2, signifying different degrees of enrichment in LREEs. These rocks also display negative Eu anomalies ($\text{Eu}/\text{Eu}^* = 0.7\text{--}0.8$) (Figure 9(1)). In addition, they show negative anomalies in Nb, Ta, and Ti, along with positive anomalies in Rb, Th, U, K, and Pb (Figure 9(2)).

The southern Qingshan biotite granodiorites have SiO_2 contents (65.11–66.61 wt%), moderate total alkali and Al_2O_3 (15.03–16.45 wt%) contents, and slightly low TFe_2O_3 (4.32–5.25 wt%) and MgO (1.61–2.41 wt%) contents with Mg# values of 42 to 48 (Figures 7 and 8). They are enriched in K_2O with $\text{K}_2\text{O}/\text{Na}_2\text{O}$ ratios varying from 0.9 to 1.3, falling into the high-K calc-alkaline series (Figure 7(2)). Moreover, they show characteristics of metaluminous (Figure 7(3)). These rocks display negative to no anomalies of Eu ($\text{Eu}/\text{Eu}^* = 0.7\text{--}1.0$) and varying degrees of enrichment in LREEs with $(\text{La}/\text{Yb})_N$ ratios ranging from 3.7 to 11.2 (Figure 9(1)). Additionally, these rocks have positive anomalies for Rb, Th, U, K, and Pb and negative anomalies for Nb, Ta, and Ti (Figure 9(2)).

4.3. Whole-Rock Sr-Nd Isotope Compositions

Whole-rock Sr-Nd isotope compositions are shown in Supplementary Table S5. Initial $^{87}\text{Sr}/^{86}\text{Sr}$ ratios and $\epsilon_{\text{Nd}}(t)$ values were calculated based on their zircon U-Pb ages, as shown in Section 3.1. The northern Qingshan diorites present $^{87}\text{Sr}/^{86}\text{Sr}$ ratios ranging from 0.7060 to 0.7061 and $\epsilon_{\text{Nd}}(t)$ values from -1.4 to -1.7 (Figure 10). The Heishantou quartz diorites show $^{87}\text{Sr}/^{86}\text{Sr}$ ratios of 0.7048 to 0.7050 and $\epsilon_{\text{Nd}}(t)$ values varying from -1.5 to 0.9 (Figure 10). The southern Qingshan biotite granodiorites present $^{87}\text{Sr}/^{86}\text{Sr}$ ratios ranging from 0.7054 to 0.7061 and $\epsilon_{\text{Nd}}(t)$ values varying from -2.0 to -1.6 (Figure 10).

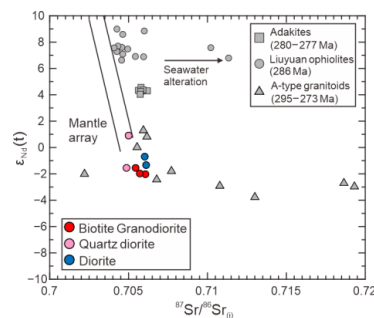


Figure 10. $\epsilon_{\text{Nd}}(t)$ vs. $^{87}\text{Sr}/^{86}\text{Sr}$ diagram. Data for the adakites (280–277 Ma) are from [16]. The data for Liuyuan ophiolites (286 Ma) are from [17]. Data for A-type granitoids (295–273 Ma) are from [19,72].

5. Discussion

5.1. Petrogenesis

5.1.1. The Northern Qingshan Diorites

The northern Qingshan diorites exhibit low SiO_2 , high Al_2O_3 , TFe_2O_3 , and CaO , and moderate K_2O and Na_2O contents, resembling the characteristics of the Setouchi sanukitoid suite (Figures 7 and 8). Additionally, they demonstrate similar REE and trace element distribution patterns to the Setouchi and central Beishan sanukitoids (Figure 9). However, these rocks exhibit slightly low MgO (4.46–4.53 wt%) contents with $\text{Mg}\#$ values of 50 to 52 and significantly low Cr (18.1–31.4 ppm) and Ni (6.87–7.74 ppm) contents when compared to these sanukitoids (Figure 11(1–3)). Consequently, the northern Qingshan diorites should be normal calc-alkaline series rocks (Figure 7(2)). Their potential origins include (1) a magma mixing process between mafic and felsic magmas [73], (2) the partial melting of mafic crustal rocks [74,75], and (3) the fractional crystallization of mantle-derived mafic magma [22]. First, the absence of mafic enclaves in the diorites and their limited range of Sr-Nd-Hf isotopes (Figures 10 and 12) do not support the existence of a magma mixing process [23,76]. Furthermore, experimental research has demonstrated that the partial melting of mafic rocks can generate calc-alkaline intermediate melts ($\text{SiO}_2 < 58 \text{ wt}\%$) [67,75,77]. These intermediate melts coexist with granulite residues below approximately 1.0 GPa and with garnet-bearing granulite or eclogite residues at higher pressures [67]. The studied diorites show high Y contents (17.8–19.1 ppm) and flat HREE patterns with low $(\text{La}/\text{Yb})_{\text{N}}$ ratios of 5.9 to 6.2 (Figure 9(1)). If the diorites are formed through the partial melting process, these features preclude the involvement of garnet in the residues during partial melting, indicating a relatively low melting pressure (<1.0 GPa). At low pressures, the partial melting of metabasaltic rocks always yields intermediate melts with high Na_2O (>4.38 wt%) and low $\text{Mg}\#$ values (<50) [67,75,78], which are not shown by the diorites from the northern Qingshan (Figures 8(5) and 11(1)). Therefore, it is inferred that the partial melting of crustal rocks cannot account for the formation of the northern Qingshan diorites.

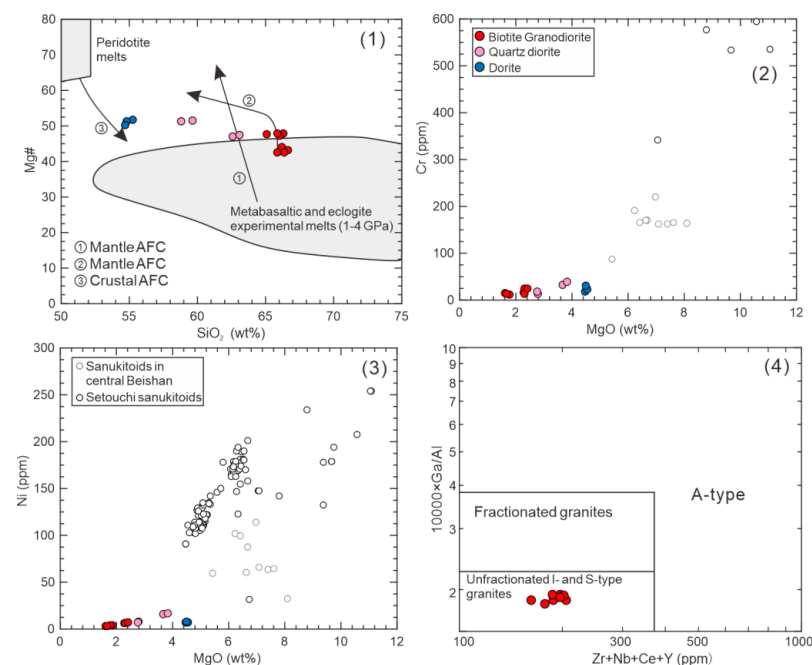


Figure 11. (1) $\text{Mg}\#$ vs. SiO_2 diagram. $\text{Mg}\# = 100 \times \text{Mg}^{2+} / (\text{Mg}^{2+} + \text{Fe}^{2+})$. Data for metabasaltic and eclogite experimental melts (1–4.0 GPa) are from the same source as those in Figure 8(2). Arrows 1 and 3 are after [79]; arrow 2 is after [68]. (2) Cr vs. MgO diagram. (3) Ni vs. MgO diagram. Data for the Setouchi and central Beishan sanukitoids are from the same source as those in Figure 8. (4) $10,000 \times \text{Ga}/\text{Al}$ vs. $\text{Zr} + \text{Nb} + \text{Ce} + \text{Y}$ diagram [80].

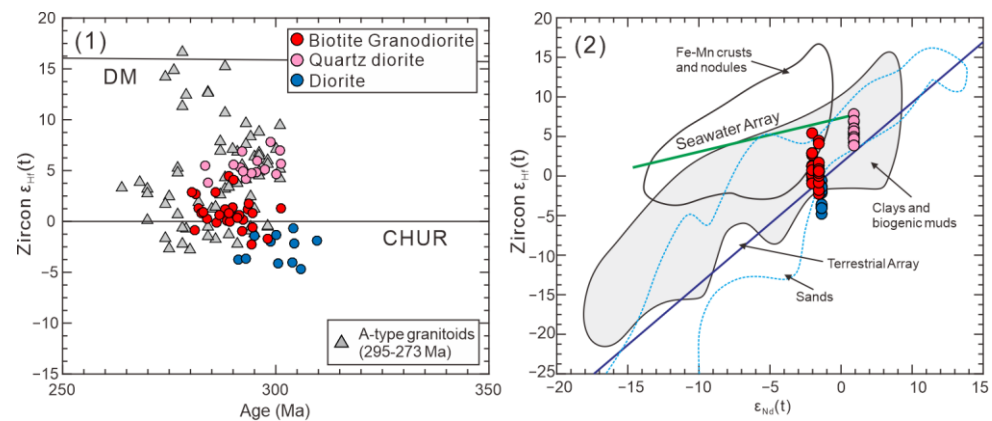


Figure 12. (1) Zircon $\epsilon_{Hf}(t)$ vs. age (Ma) diagram. Data for A-type granitoids (295–273 Ma) are from the same source as those in Figure 10. (2) Zircon $\epsilon_{Hf}(t)$ vs. the whole-rock $\epsilon_{Nd}(t)$ diagram. The fields of oceanic sediments, including deep-sea clays and biogenic muds, Fe-Mn crusts and nodules, and sands, the seawater array, and the terrestrial array are from [81,82].

Alternatively, the diorites likely formed through the fractional crystallization of mantle-derived magma. In the Mg# vs. SiO_2 diagram (Figure 11(1)), they are plotted near the trend associated with the crustal assimilation–fractional crystallization (AFC) of mantle-derived melts. Moreover, their significantly lower Cr and Ni contents and Mg# values compared to those of mantle-derived mafic magma ($Ni > 150$ ppm; $Mg\# > 65$) [83] suggest the extensive fractionation of the mafic magma [22,84]. Additionally, these rocks exhibit enrichments in LREEs relative to HREEs, positive anomalies in Rb, Th, U, K, and Pb, and negative anomalies in Nb and Ta (Figure 9). Together with their enrichment in whole-rock Sr–Nd isotopes ($^{87}Sr/^{86}Sr = 0.7060–0.7061$; $\epsilon_{Nd}(t) = -1.4–-1.7$) and zircon Hf isotopes ($\epsilon_{Hf}(t) = -4.7$ to -0.6) (Figures 10 and 12), we infer that they were sourced from an enriched mantle. The component with enriched compositions can be introduced to mantle-derived magma, either through slab-derived materials (source contamination) or through the overriding continental crust (path contamination) [85]. Here, it is difficult to quantify the relative contributions of source and path contamination in the enriched mantle source proposed for the northern Qingshan diorites due to the lack of detailed knowledge of different end components. We prefer to suggest that the slab-derived fluids/melts likely play a crucial role in forming the enriched mantle source, as indicated by the absence of wall-rock xenoliths and the ancient inherited zircon in the studied diorites. Moreover, both Ba and Th elements are mobile and tend to show high contents in subduction-related fluids/melts [86]. The diorites display high Th/Yb and low La/Ba ratios, implying the influence of slab-derived materials in their magma source. In summary, we infer that the northern Qingshan diorites likely originate from an enriched mantle modified by subduction-related components.

5.1.2. The Heishantou Quartz Diorites

The Heishantou quartz diorites are coeval with the northern Qingshan diorites discussed above, and they define curvilinear and/or linear compositional trends for major elements with increasing SiO_2 contents (Figure 8), which may suggest that the fractional crystallization process dominantly contributed to their generation [87]. However, the quartz diorites show a slight depletion in whole-rock Sr–Nd ($^{87}Sr/^{86}Sr = 0.7048–0.7050$; $\epsilon_{Nd}(t) = -1.5–+0.9$) and zircon Hf ($\epsilon_{Hf}(t) = 3.8–7.8$) isotope compositions than those of the diorites (Figures 10 and 12). This precludes the possibility of a magma fractionation process. Moreover, geochemical modeling suggests that fractional crystallization would yield an almost horizontal line in plots of incompatible trace elements with different bulk partition coefficients, while partial melting and magma mixing would produce a straight line with a slope [88]. In the Th/Nd vs. Th diagram (Figure 13(1)), the quartz diorites and diorites do not define such a trend, which is inconsistent with a magma fractionation process.

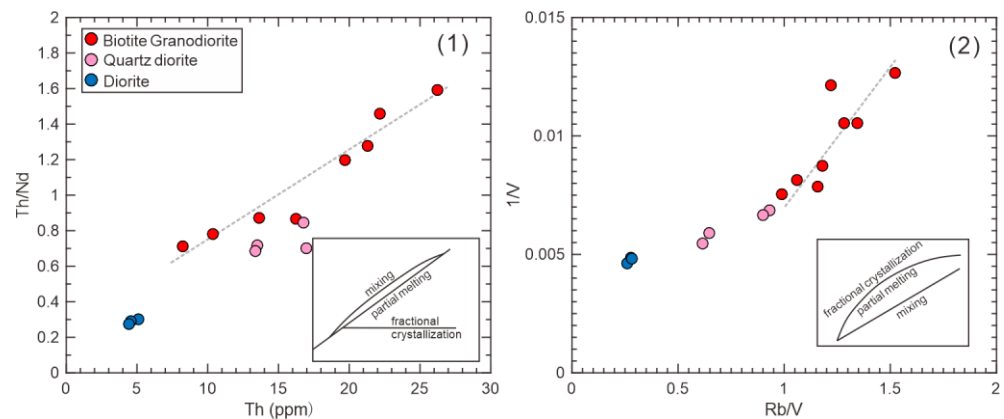


Figure 13. (1) Th/Nd vs. Th and (2) 1/V vs. Rb/V diagrams [88].

The calc-alkaline quartz diorites have SiO₂ contents of 58.79 to 63.08 wt% and MgO contents of 2.75 to 3.84 wt% (Figure 8). In the Mg# vs. SiO₂ diagram (Figure 11(1)), these rocks are plotted near the area of experimental melts of crustal rocks and tend to have higher Mg# values with decreasing SiO₂ contents. This observation indicates that quartz diorites likely represent crustal-derived magma with varying degrees of input from mantle-derived mafic melts. Among the quartz diorites, those with higher SiO₂ (59.61 wt%) show an enrichment in the Nd isotope composition ($\epsilon_{\text{Nd}}(t) = -1.5$) compared to less mafic rocks (SiO₂ = 62.57 wt%; $\epsilon_{\text{Nd}}(t) = 0.9$) (Supplementary Table S5). Therefore, the mafic magma that was involved in the formation of quartz diorites should be sourced from enriched mantle materials. Furthermore, the quartz diorites are all characterized by a slight depletion in Sr-Nd-Hf isotopes (Figures 10 and 12), indicating a juvenile lower crust. Additionally, they are enriched in LREEs relative to HREEs and display positive anomalies of Rb, Th, U, K, and Pb, as well as negative anomalies of Nb and Ta (Figure 9), showing the signatures of arc-like magmatism.

Generally, Nd and Hf isotopes of most crustal and mantle-derived rocks form the “Terrestrial Array” due to the similar fractionation of Sm/Nd and Lu/Hf ratios during magma evolution [82]. However, oceanic sediments, such as Fe-Mn crusts and nodules, sea clays, and biogenic muds, are typically enriched in trace elements (e.g., Sm, Nd, and Lu) and tend to have higher Lu/Hf ratios, resulting in high ϵ_{Hf} values at given ϵ_{Nd} values (Figure 12(2)) [82]. In the zircon $\epsilon_{\text{Hf}}(t)$ vs. the whole-rock $\epsilon_{\text{Nd}}(t)$ diagram (Figure 12(2)), the quartz diorites are plotted over the terrestrial array line, suggesting that oceanic sediments from a subducted slab probably modified the mantle source where partial melting occurred to form the juvenile lower crust mentioned above. Additionally, the breakdown of garnet during crustal melting under high pressures can yield melts with elevated HREE contents, leading to high Lu/Hf ratios and $\epsilon_{\text{Hf}}(t)$ values in derived melts [89]. However, the quartz diorites show high Y contents (20.0–21.0 ppm) and flat HREE patterns with (La/Yb)_N ratios of 6.0 to 17.2, which do not support the existence of garnet during their formation. The mechanism of the disequilibrium melting of zircon during the crustal melting process is also utilized to explain Nd-Hf isotope decoupling, as residual zircon can retain ¹⁷⁷Hf and, thus, generate high ¹⁷⁶Hf/¹⁷⁷Hf in melts [90]. However, the quartz diorites show positive Zr-Hf anomalies (Figure 9(2)) and high Zr contents (94.3–158 ppm). Together with the absence of inherited zircons, we infer that residual zircons do not substantially exist, precluding the possibility of zircon disequilibrium melting [91]. In summary, the Heishantou quartz diorites were derived from the partial melting of the juvenile lower crust, previously influenced by oceanic sediments, with the involvement of enriched mantle-derived magma.

5.1.3. The Southern Qingshan Biotite Granodiorites

The southern Qingshan biotite granodiorites exhibit moderate SiO₂ contents (65.11–66.61 wt%) and contain amphibole in their mineral assemblages (Figure 3(6)), together with their metaluminous characteristics (A/CNK = 0.91–0.97) (Figure 7(3)), which

indicate I-type affinities for these rocks [92,93]. The low $10,000 \times \text{Ga}/\text{Al}$ (1.8–1.9) ratios (Figure 11(4)) and Ti-in-zircon temperature (647–790 °C, average 711 °C) further confirm their classification as I-type granitoids [80,94,95]. Additionally, these rocks show high K_2O contents (2.88–3.70 wt%) with high $\text{K}_2\text{O}/\text{Na}_2\text{O}$ ratios (0.9–1.3), belonging to the high-K calc-alkaline series (Figure 7(2)). High-K calc-alkaline I-type granitoid can form via the (1) fractional crystallization of mantle-derived alkaline mafic melts [96], (2) the partial melting of mafic-intermediate metaigneous rocks with transitional to high K calc-alkaline characteristics [97], and (3) magma mixing between crustal- and mantle-derived melts [98]. The absence of coeval cogenetic mafic rocks and associated cumulates in the regional context precludes the possibility of the fractionation process. The biotite granodiorites show enrichment in whole-rock Sr-Nd isotope compositions ($^{87}\text{Sr}/^{86}\text{Sr} = 0.7054\text{--}0.7061$; $\epsilon_{\text{Nd}}(t) = -2.0\text{--}1.6$) (Figure 10), which may indicate a uniform crustal source. However, their zircon Hf isotopes are variable, with $\epsilon_{\text{Hf}}(t)$ values ranging from -2.3 to $+4.5$ (Figure 12(1)). Mafic enclaves are commonly present in the southern Qingshan pluton (Figure 3(3)). They exhibit an igneous texture and zircon U-Pb age (274 Ma), similar to the host biotite granodiorites [12]. The mafic enclaves show lower SiO_2 (46.42 wt%) and high MgO contents (5.52 wt%), together with their arc geochemical signatures [12], implying that they originated from the enriched mantle. Moreover, the enclaves also present variable $\epsilon_{\text{Hf}}(t)$ values of -1.3 to 5.1 [12], indicating that they were modified by the host rocks. In the MgO and Mg# vs. SiO_2 diagrams, the biotite granodiorites plot in the area of experimental crustal melts, and some rocks exhibit a higher MgO and Mg# than those of these melts (Figures 8(3) and 11(1)), suggesting the involvement of mafic magma. All these data imply the key role of the magma mixing process in the formation of the biotite granodiorites [23,99]. In the Th/Nd vs. Th diagram (Figure 13(1)), these rocks follow the geochemical trend of partial melting or magma mixing processes. Additionally, previous studies have shown that the magma mixing process tends to be expressed by an almost straight line in one compatible vs. one incompatible element diagram [88]. In the 1/V vs. Rb/V diagram, the biotite granodiorites define a straight line with a slope, which is consistent with the magma mixing process. Therefore, the geochemical features of trace elements further support the inference of magma mixing.

The mafic enclaves likely approached the composition of the mafic end member, although they were influenced by the host biotite granodiorites. The felsic end member was probably sourced from the juvenile lower crust. In the zircon $\epsilon_{\text{Hf}}(t)$ vs. whole-rock $\epsilon_{\text{Nd}}(t)$ diagram (Figure 12(2)), the biotite granodiorites lie on or above the terrestrial array. As discussed in Section 5.1.2, several factors, including the effect of garnet, zircon, and oceanic sediments, can lead to higher $\epsilon_{\text{Hf}}(t)$ at given $\epsilon_{\text{Nd}}(t)$ values [100]. First, the effect of garnet can be ruled out based on the high Y contents (14.0–19.6 ppm) and flat HREE patterns ($(\text{La}/\text{Yb})_{\text{N}} = 3.7$ to 11.2). Second, the effect of zircon is also improbable. These rocks have high Zr contents (106–142 ppm) and positive Zr-Hf anomalies, which do not indicate the substantial occurrence of residual zircons during the process of crustal partial melting. Therefore, we infer that the juvenile lower crust was probably sourced from oceanic sediment-modified mantle materials. In summary, the magma mixing process played a vital role in the formation of the southern Qingshan biotite granodiorites. Two end member magmas were involved as follows: one derived from an enriched mantle and the other from a preexisting juvenile lower crust.

5.2. Implications for the Early Permian Geodynamic Setting in the Southern Beishan

The Shibanshan unit, situated at the southernmost end of the Beishan orogen, occupies a key location for understanding the final amalgamation of this orogen [8]. Permian igneous rocks are widely developed, and their compositions range from mafic to felsic (Figure 2) (Supplementary Table S1). Previous studies propose that the early Permian mafic-ultramafic rocks in the Beishan orogen formed in a rifting tectonic setting related to the early Permian Tarim mantle plume [18,101]. However, the distribution pattern of early Permian mafic rocks in the Shibanshan unit, along the Liuyuan ophiolitic mélange belt

(Figure 2), contradicts the planar distribution typically observed in mantle plume-associated igneous rocks [16,102]. Furthermore, some authors argue that these rocks exhibit distinct whole-rock trace element characteristics from those in the Tarim Large Igneous Province (LIP) [16]. Additionally, Permian (281–265 Ma) mafic igneous rocks in the Shibanshan unit were considered to be sourced from mantle materials influenced by subduction-related fluids/melts [103]. Collectively, these data do not support the existence of a mantle plume during the early Permian in the Shibanshan unit.

Additionally, a post-collisional setting [20,31] or continental arc setting [16,33] was suggested to account for the formation of the early Permian igneous rocks in southern Beishan. We preclude the possibility of a post-collisional setting based on several reasons. First, the Liuyuan complex to the north of the Shibanshan unit developed a large volume of MORB-type ophiolitic blocks during the early Permian to Late Triassic, which means that the Liuyuan Ocean still existed in that period [17,33]. Second, the high-Mg diorite and gabbro dikes showing arc-like geochemical features, along with adakitic-like granites, suggest the ongoing southward subduction of the Liuyuan Ocean during the middle Permian (269–267 Ma) [16]. Third, our study reveals that the early Permian intermediate–felsic rocks in the Shibanshan unit exhibit geochemical signatures of arc igneous rocks, and subduction-related components were involved in their generation. Finally, zircon trace element-based diagrams were constructed to discriminate the mid-ocean ridge, plume-influenced ocean island, and subduction-related arc environments [58]. All the analyzed zircons from the three plutons in the Shibanshan unit plot were within and/or near the continental arc-type zircon field (Figure 14). These findings suggest that a continental arc setting is more feasible for the early Permian magmatism in the Shibanshan unit.

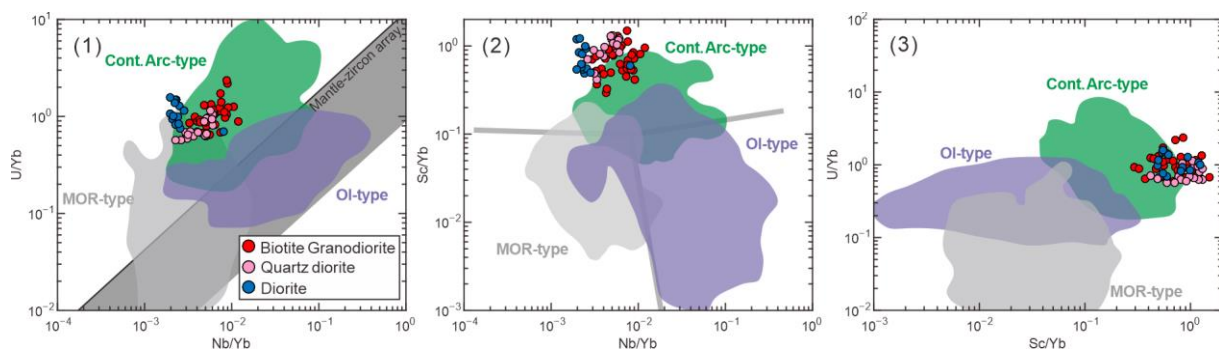


Figure 14. Tectonic discrimination diagrams based on zircon trace elements [76]. (1) U/Yb vs. Nb/Yb, (2) Sc/Yb vs. Nb/Yb, and (3) U/Yb vs. Sc/Yb. Con.Arc-type: continental arc-type; MOR-type: mid-ocean ridge-type; OI-type: ocean island-type.

Furthermore, our study reveals the involvement of different magma components in the formation of early Permian intermediate–felsic rocks, indicating the interaction between crustal- and mantle-derived magma. Early-mid Permian (295–273 Ma) granitoids with A-type affinities were documented in the Shibanshan unit [19,72]. The occurrence of A-type granitoids most likely indicates an extensional setting, where crustal source rocks experienced partial melting under relatively high temperatures and low pressures [94,104]. These A-type granitoids show many variable whole-rock Sr-Nd and zircon Hf isotope compositions (Figures 10 and 12), suggesting strong interaction between the depleted mantle and/or juvenile lower crust and ancient crustal rocks. Here, we propose a retreating subduction zone developed in the Shibanshan unit during the early Permian period (Figure 15). Retreating subduction occurs where the rate of rollback of the subducted slab is greater than the rate of advance of the overriding plate, leading to crustal extension in the latter [105]. The extensional regime within the overriding continental arc likely facilitated the generation of A-type granitoids in the Shibanshan unit (Figure 15) [106]. Additionally, during retreating subduction, the upwelling hot asthenospheric mantle can cause the partial melting of overriding crustal rocks, in which mantle materials can be

involved, producing the strong crust–mantle interaction discussed above. In summary, it is inferred that the retreating subduction of the Liuyuan Ocean produced the early Permian intermediate–felsic magmatism in the Shibanshan unit (Figure 15).

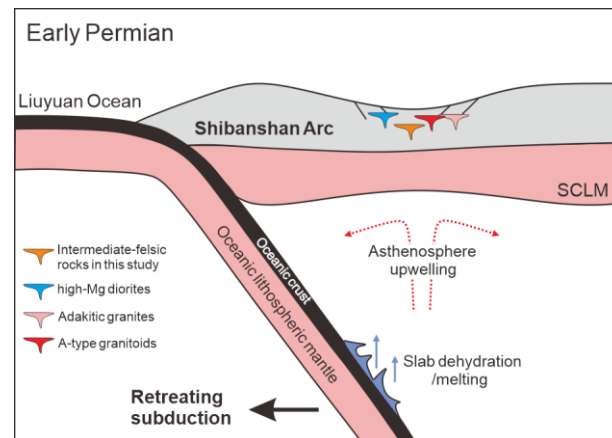


Figure 15. A tectonic model for early Permian magmatism in southern Beishan. High-Mg diorites and adakitic granites are from [16]. A-type granitoids are from [19,72]. Abbreviations: SCLM—subcontinental lithospheric mantle.

The Beishan orogen comprises five tectonic units separated by four east–west oriented ophiolitic mélangé belts (Figure 1(2)). The nature and timing of these mélangé belts remain under debate, and different tectonic models have been proposed to account for the formation of the Beishan orogen [35,107]. Primarily based on studies of volcano–sedimentary successions, some authors argue that the Jijitai–Xiaohuangshan mélangé belt may represent a major branch of the PAO and that the Beishan orogen evolved into a continental rift setting following the closure of this ocean around the Early Devonian [108,109]. However, this mélangé belt formed in the Ordovician–early Carboniferous period (480 to 321 Ma), as revealed by LA-ICP-MS zircon U–Pb dating results [35,110], and is thought to have formed in a back-arc setting [14,32]. The Hongliuhe–Niujuanzi–Xichangjing mélangé belt shows zircon U–Pb ages ranging from 536 to 426 Ma [35], and the ocean it represents is thought to have closed before the Early Devonian [111,112]. The development of the Early Devonian S- and A-type granites in central Beishan orogen further supports this inference [113]. Additionally, the Hongshishan mélangé belt, situated in the northernmost part of the Beishan orogen, was formed in the Carboniferous–early Permian period (357–297 Ma) according to zircon U–Pb dating results [35]. Coeval arc calc-alkaline magmatism in the Heiyingshan–Hanshan unit also indicates the existence of the southward subduction of the ocean represented by the Hongshishan mélangé belt [114,115]. The early Permian (289 Ma) alkali feldspar granites in the Hongshishan area are considered to have formed in a post-collisional setting [116], implying that the Hongshishan Ocean probably closed before the middle Permian [117,118]. Furthermore, the oceanic blocks from the Liuyuan mélangé belt, located in the southernmost part of the Beishan orogen, show zircon U–Pb ages spanning the Cambrian–Permian period (540–270 Ma) [17,33]. Our study also demonstrates that the Liuyuan Ocean still existed during the early Permian. The final closure of this ocean may be later than 234 Ma, as indicated by the age of the sedimentary matrix from the Liuyuan complex [33]. To summarize, the existence of the late Paleozoic ophiolitic mélangés and arc magmatism likely implies that the Beishan orogen formed through multiple accretionary–collisional processes during the Paleozoic. The Liuyuan ophiolitic mélangé belts may represent the site of the final closure of the PAO in the Beishan orogen.

6. Conclusions

- (1) Intermediate–felsic igneous rocks are widespread in the Shibanshan unit, the southernmost end of the Beishan orogen. New LA-ICP-MS zircon U–Pb results reveal

ages of 300 Ma for the northern Qingshan diorites, 294 Ma for the Heishantou quartz diorites, and 291–286 Ma for the southern Qingshan biotite granodiorites. The diorites were likely sourced from an enriched mantle influenced by subduction fluids and/or melts. The quartz diorites originated from the partial melting of the juvenile lower crustal rocks with input from the enriched mantle. The biotite granodiorites are I-type granitoids and originated from a mixing process between the enriched mantle-derived and preexisting juvenile lower crust-derived magmas.

- (2) The early Permian intermediate–felsic rocks exhibit geochemical signatures of arc magmatism, and their generation involved subduction-related materials. Different magma components, including the enriched mantle and juvenile lower crust, participated in the generation of these rocks, implying a strong interaction between crustal- and mantle-derived magmas. Additionally, all analyzed zircons in this study exhibit trace element characteristics typical of continental arc-type zircons. In conjunction with previous studies, we infer that an early Permian retreating subduction of the Liuyuan Ocean developed in the Shibanshan unit, the southernmost part of the Beishan orogen. Moreover, the Beishan orogen likely experienced multiple accretionary–collisional processes during the Paleozoic.

Supplementary Materials: The following supporting information can be downloaded at: <https://www.mdpi.com/article/10.3390/min14010114/s1>, Figure S1: Chondrite-normalized REE patterns of analyzed zircons in this study; Table S1: Compiled zircon U–Pb age data of igneous rocks in the study area [16,38,118–140]; Table S2: LA–ICP–MS zircon U–Pb age and rare earth element data of the igneous rocks in this study; Table S3: LA–MC–ICP–MS zircon Lu–Hf isotope data of igneous rocks in this study; Table S4: Whole-rock major and trace element data of igneous rocks in this study; Table S5: Whole-rock Sr–Nd isotopes of igneous rocks in this study.

Author Contributions: Conceptualization, R.L. (Runwu Li) and S.S.; Data curation, R.L. (Runwu Li) and R.L. (Ruibin Liu); Funding acquisition, S.S. and H.S.; Investigation, R.L. (Runwu Li), H.S., R.L., (Ruibin Liu) and Y.X.; Supervision, S.S. and H.S.; Writing—original draft, R.L. (Runwu Li); Writing—review and editing, S.S. and H.S. All authors have read and agreed to the published version of the manuscript.

Funding: This work was supported by the National Natural Science Foundation of China (41830216, U2244217, 92162213), projects of the China Geological Survey (DD20221647, DD20190685), and the National Key Research and Development Program of China (2018YFC0603702). This publication contributes to DDE and IGCP-662.

Data Availability Statement: The original contributions presented in the study are included in the article/Supplementary Material.

Acknowledgments: We greatly thank the editors and four anonymous reviewers for their valuable comments and suggestions. We are grateful to Qian Tian and Wei-Wei Li for their help with the fieldwork.

Conflicts of Interest: The authors declare no conflicts of interest.

References

1. Sengör, A.M.C.; Natalin, B.A.; Burtman, V.S. Evolution of the Altaid tectonic collage and Palaeozoic crustal growth in Eurasia. *Nature* **1993**, *364*, 299–307. [[CrossRef](#)]
2. Jahn, B.M.; Wu, F.Y.; Chen, B. Granitoids of the Central Asian Orogenic Belt and continental growth in the Phanerozoic. *Trans. R. Soc. Edinb. Earth Sci.* **2000**, *91*, 181–193. [[CrossRef](#)]
3. Xiao, W.J.; Windley, B.F.; Sun, S.; Li, J.L.; Huang, B.C.; Han, C.M.; Yuan, C.; Sun, M.; Chen, H.L. A Tale of Amalgamation of Three Permo-Triassic Collage Systems in Central Asia: Oroclines, Sutures, and Terminal Accretion. *Annu. Rev. Earth Planet. Sci.* **2015**, *43*, 477–507. [[CrossRef](#)]
4. Wang, T.; Xiao, W.J.; Collins, W.; Tong, Y.; Hou, Z.Q.; Huang, H.; Xiaoxia, W.; Lin, S.F.; Seltmann, R.; Wang, C.Y.; et al. Quantitative characterization of orogens through isotopic mapping. *Commun. Earth Environ.* **2023**, *4*, 110. [[CrossRef](#)]
5. Yakubchuk, A.S.; Shatov, V.V.; Kirwin, D.; Edwards, A.; Tomurtogoo, O.; Badarch, G.; Buryak, V.A. Gold and base metal metallogeny of the Central Asian orogenic supercollage. In *Economic Geology 100th Anniversary Volume*; Hedenquist, J.W., Thompson, J.F.H., Goldfarb, R.J., Richards, J.P., Eds.; Society of Economic Geologists: Littleton, CO, USA, 2005; pp. 1035–1068.

6. Gao, J.; Klemd, R.; Zhu, M.; Wang, X.; Li, J.; Wan, B.; Xiao, W.; Zeng, Q.; Shen, P.; Sun, J.; et al. Large-scale porphyry-type mineralization in the Central Asian metallogenic domain: A review. *J. Asian Earth Sci.* **2018**, *165*, 7–36. [[CrossRef](#)]
7. Heinhorst, J.; Lehmann, B.; Ermolov, P.; Serykh, V.; Zhurutin, S. Paleozoic crustal growth and metallogeny of Central Asia: Evidence from magmatic-hydrothermal ore systems of Central Kazakhstan. *Tectonophysics* **2000**, *328*, 69–87. [[CrossRef](#)]
8. Xiao, W.J.; Mao, Q.G.; Windley, B.F.; Han, C.M.; Qu, J.F.; Zhang, J.E.; Ao, S.J.; Guo, Q.Q.; Cleven, N.R.; Lin, S.F. Paleozoic multiple accretionary and collisional processes of the Beishan orogenic collage. *Am. J. Sci.* **2010**, *310*, 1553–1594. [[CrossRef](#)]
9. Metcalfe, I. Multiple Tethyan ocean basins and orogenic belts in Asia. *Gondwana Res.* **2021**, *100*, 87–130. [[CrossRef](#)]
10. Wu, F.Y.; Wan, B.; Zhao, L.; Xiao, W.J.; Zhu, R.X. Tethyan geodynamics. *Acta Petrol. Sin.* **2020**, *36*, 1627–1674. (In Chinese with English abstract)
11. Wang, X.Y. The Rock Assemblages, Spatial and Temporal Variations in the Gongpoquan Arc, Beishan and Their Implications for Tectonic Setting. Ph.D. Thesis, Guangzhou Institute of Geochemistry, GAS, Guangzhou, China, 2017; 149p.
12. Yuan, Y. The Continental Crust Formation and Evolution of the Beishan Orogenic Belt. Ph.D. Thesis, China University of Geosciences, Wuhan, China, 2019; 255p.
13. Zheng, R.G.; Xiao, W.J.; Li, J.Y.; Wu, T.R.; Zhang, W. A Silurian-early Devonian slab window in the southern Central Asian Orogenic Belt: Evidence from high-Mg diorites, adakites and granitoids in the western Central Beishan region, NW China. *J. Asian Earth Sci.* **2018**, *153*, 75–99. [[CrossRef](#)]
14. Song, D.F.; Xiao, W.J.; Windley, B.F.; Han, C.M.; Tian, Z.H. A Paleozoic Japan-type subduction-accretion system in the Beishan orogenic collage, southern Central Asian Orogenic Belt. *Lithos* **2015**, *224–225*, 195–213. [[CrossRef](#)]
15. Wang, E.; Zhai, X.; Chen, W.; Wu, L.; Song, G.; Wang, Y.; Guo, Z.; Zhao, J.; Wang, J. Late Devonian A-Type Granites from the Beishan, Southern Central Asia Orogenic Belt: Implications for Closure of the Paleo-Asia Ocean. *Minerals* **2023**, *13*, 565. [[CrossRef](#)]
16. Zheng, R.G.; Li, J.Y.; Zhang, J.; Xiao, W.J.; Wang, Q.J. Permian oceanic slab subduction in the southmost of Central Asian Orogenic Belt: Evidence from adakite and high-Mg diorite in the southern Beishan. *Lithos* **2020**, *358*, 105406. [[CrossRef](#)]
17. Mao, Q.G.; Xiao, W.J.; Windley, B.F.; Han, C.M.; Qu, J.F.; Ao, S.J.; Zhang, J.E.; Guo, Q.Q. The Liuyuan complex in the Beishan, NW China: A Carboniferous–Permian ophiolitic fore-arc sliver in the southern Altai. *Geol. Mag.* **2012**, *149*, 483–506. [[CrossRef](#)]
18. Su, B.-X.; Qin, K.-Z.; Sakyi, P.A.; Li, X.-H.; Yang, Y.-H.; Sun, H.; Tang, D.-M.; Liu, P.-P.; Xiao, Q.-H.; Malaviarachchi, S.P.K. U–Pb ages and Hf–O isotopes of zircons from Late Paleozoic mafic–ultramafic units in the southern Central Asian Orogenic Belt: Tectonic implications and evidence for an Early-Permian mantle plume. *Gondwana Res.* **2011**, *20*, 516–531. [[CrossRef](#)]
19. Zhang, W.; Wu, T.; Zheng, R.; Feng, J.; Luo, H.; He, Y.; Xu, C. Post-collisional Southeastern Beishan granites: Geochemistry, geochronology, Sr–Nd–Hf isotopes and their implications for tectonic evolution. *J. Asian Earth Sci.* **2012**, *58*, 51–63. [[CrossRef](#)]
20. Niu, Y.Z.; Shi, G.R.; Wang, J.Q.; Liu, C.Y.; Zhou, J.L.; Lu, J.C.; Song, B.; Xu, W. The closing of the southern branch of the Paleo-Asian Ocean: Constraints from sedimentary records in the southern Beishan Region of the Central Asian Orogenic Belt, NW China. *Mar. Pet. Geol.* **2021**, *124*, 104791. [[CrossRef](#)]
21. Moyon, J.F.; Laurent, O.; Chelle-Michou, C.; Couzinié, S.; Vanderhaeghe, O.; Zeh, A.; Villaros, A.; Gardien, V. Collision vs. subduction-related magmatism: Two contrasting ways of granite formation and implications for crustal growth. *Lithos* **2017**, *277*, 154–177. [[CrossRef](#)]
22. Marxer, F.; Ulmer, P.; Müntener, O. Polybaric fractional crystallisation of arc magmas: An experimental study simulating trans-crustal magmatic systems. *Contrib. Mineral. Petrol.* **2021**, *176*, 3. [[CrossRef](#)]
23. Barbarin, B. Mafic magmatic enclaves and mafic rocks associated with some granitoids of the central Sierra Nevada batholith, California: Nature, origin, and relations with the hosts. *Lithos* **2005**, *80*, 155–177. [[CrossRef](#)]
24. DePaolo, D.J. Trace element and isotopic effects of combined wallrock assimilation and fractional crystallization. *Earth Planet. Sci. Lett.* **1981**, *53*, 189–202. [[CrossRef](#)]
25. Webster, J.D. Exsolution of magmatic volatile phases from Cl-enriched mineralizing granitic magmas and implications for ore metal transport. *Geochim. Cosmochim. Acta* **1997**, *61*, 1017–1029. [[CrossRef](#)]
26. Charlier, B.; Grove, T.L. Experiments on liquid immiscibility along tholeiitic liquid lines of descent. *Contrib. Mineral. Petrol.* **2012**, *164*, 27–44. [[CrossRef](#)]
27. Clemens, J.D.; Stevens, G. What controls chemical variation in granitic magmas? *Lithos* **2012**, *134–135*, 317–329. [[CrossRef](#)]
28. Moyon, J.-F.; Janoušek, V.; Laurent, O.; Bachmann, O.; Jacob, J.-B.; Farina, F.; Fiannacca, P.; Villaros, A. Crustal melting vs. fractionation of basaltic magmas: Part 1, granites and paradigms. *Lithos* **2021**, *402–403*, 106291. [[CrossRef](#)]
29. Chapman, J.B.; Ducea, M.N.; Kapp, P.; Gehrels, G.E.; DeCelles, P.G. Spatial and temporal radiogenic isotopic trends of magmatism in Cordilleran orogens. *Gondwana Res.* **2017**, *48*, 189–204. [[CrossRef](#)]
30. Zhu, D.C.; Wang, Q.; Weinberg, R.; Cawood, P.; Chung, S.L.; Zheng, Y.F.; Zhao, Z.; Hou, Z.Q.; Mo, X.X. Interplay between oceanic subduction and continental collision in building continental crust. *Nat. Commun.* **2022**, *13*, 7141. [[CrossRef](#)]
31. Zuo, G.C.; He, G.Q. *Plate Tectonics and Metallogenesis Regularities in Beishan Region*; Peking University Press: Beijing, China, 1990.
32. Yang, H.Q.; Li, Y.; Zhao, G.B.; Li, W.Y.; Wang, X.H.; Jiang, H.B.; Tan, W.J.; Sun, N.Y. Character and Structural Attribute of the Beishan Ophiolite. *Northwestern Geol.* **2010**, *43*, 26–36. (In Chinese with English abstract)
33. Mao, Q.G.; Xiao, W.J.; Wang, H.; Ao, S.J.; Windley, B.; Song, D.F.; Sang, M.; Tan, Z.; Li, R.; Wang, M. Prolonged Late Mesoproterozoic to Late Triassic Tectonic Evolution of the Major Paleo-Asian Ocean in the Beishan Orogen (NW China) in the Southern Altai. *Front. Earth Sci.* **2022**, *9*, 825852. [[CrossRef](#)]

34. Santos, G.S.; Bédard, J.; Staal, C.; Lin, S.F.; Hong, T.; Wang, K. Geology of the Liuyuan Complex, NW China: A Permian back-arc basin ophiolite at the southern edge of the Central Asian orogenic belt. *Geol. Soc. Am. Bull.* **2023**, *135*, 2830–2848. [[CrossRef](#)]
35. Wang, G.Q.; Li, X.M.; Xu, X.Y.; Yu, J.Y.; Wu, P.; Ji, B. Research status and progress of Paleozoic ophiolites in Beishan orogenic belt. *Geol. Bull. China* **2021**, *40*, 71–81. (In Chinese with English abstract)
36. Song, D.F.; Xiao, W.J.; Windley, B.F.; Han, C.M.; Yang, L. Metamorphic complexes in accretionary orogens: Insights from the Beishan collage, southern Central Asian Orogenic Belt. *Tectonophysics* **2016**, *688*, 135–147. [[CrossRef](#)]
37. He, Z.Y.; Klemd, R.; Yan, L.L.; Zhang, Z.M. The origin and crustal evolution of microcontinents in the Beishan orogen of the southern Central Asian Orogenic Belt. *Earth-Sci. Rev.* **2018**, *185*, 1–14. [[CrossRef](#)]
38. Zheng, R.; Li, J.; Zhang, J.; Xiao, W. A prolonged subduction-accretion in the southern Central Asian Orogenic Belt: Insights from anatomy and tectonic affinity for the Beishan complex. *Gondwana Res.* **2021**, *95*, 88–112. [[CrossRef](#)]
39. Castro, A. Tonalite–granodiorite suites as cotectic systems: A review of experimental studies with applications to granitoid petrogenesis. *Earth-Sci. Rev.* **2013**, *124*, 68–95. [[CrossRef](#)]
40. Yu, C.; Yang, Z.M.; Zhou, L.M.; Zhang, L.L.; Li, Z.Q.; Zhao, M.; Zhang, J.Y.; Chen, W.Y.; Suo, M.S. Impact of laser focus on accuracy of U–Pb dating of zircons by LA-ICPMS. *Miner. Depos.* **2019**, *38*, 21–28. (In Chinese with English abstract)
41. Liu, R.; Tong, Y.; Zhang, H.-F.; Duan, S.; Guo, L. Mixing of magmas from multiple sources in the petrogenesis of multi-stage Early Cretaceous syenites in the Wulingshan alkaline complex, northern North China Craton: Evidence from enclaves. *Geol. J.* **2023**, *58*, 3063–3086. [[CrossRef](#)]
42. Paton, C.; Woodhead, J.D.; Hellstrom, J.C.; Hergt, J.M.; Greig, A.; Maas, R. Improved laser ablation U–Pb zircon geochronology through robust downhole fractionation correction. *Geochem. Geophys. Geosyst.* **2010**, *11*, 1–36. [[CrossRef](#)]
43. Ludwig, K.R. Isoplot 3.00: A Geochronological Toolkit for Microsoft Excel, Berkeley. *Geochronol. Cent. Spec. Publ.* **2003**, *4*, 1–74.
44. Wu, F.Y.; Yang, Y.H.; Xie, L.W.; Yang, J.H.; Xu, P. Hf isotopic compositions of the standard zircons and baddeleyites used in U–Pb geochronology. *Chem. Geol.* **2006**, *234*, 105–126. [[CrossRef](#)]
45. Hou, K.J.; Li, Y.H.; Zou, T.R.; Qu, X.M.; Shi, Y.R.; Xie, G.Q. Laser Ablation-MC-ICP-MS technique for Hf Isotope Microanalysis of Zircon and its Geological applications. *Acta Petrol. Sin.* **2007**, *23*, 2595–2604. (In Chinese with English abstract).
46. Söderlund, U.; Patchett, P.J.; Vervoort, J.D.; Isachsen, C.E. The ¹⁷⁶Lu decay constant determined by Lu–Hf and U–Pb isotope systematics of Precambrian mafic intrusions. *Earth Planet. Sci. Lett.* **2004**, *219*, 311–324. [[CrossRef](#)]
47. Blichert-Toft, J.; Albarède, F. The Lu–Hf isotope geochemistry of chondrites and the evolution of the mantle-crust system. *Earth Planet. Sci. Lett.* **1997**, *148*, 243–258. [[CrossRef](#)]
48. Griffin, W.L.; Pearson, N.J.; Belousova, E.; Jackson, S.E.; van Achterbergh, E.; O’Reilly, S.Y.; Shee, S.R. The Hf isotope composition of cratonic mantle: LAM-MC-ICPMS analysis of zircon megacrysts in kimberlites. *Geochim. Cosmochim. Acta* **2000**, *64*, 133–147. [[CrossRef](#)]
49. Liu, Y.; Zong, K.; Kelemen, P.B.; Gao, S. Geochemistry and magmatic history of eclogites and ultramafic rocks from the Chinese continental scientific drill hole: Subduction and ultrahigh-pressure metamorphism of lower crustal cumulates. *Chem. Geol.* **2008**, *247*, 133–153. [[CrossRef](#)]
50. Savatenkov, V.M.; Kozlovsky, A.M.; Yarmolyuk, V.V.; Rudnev, S.N.; Oyunchimeg, T. Pb and Nd Isotopic Data on Granitoids from the Lake Zone, Mongolian and Gobi Altai with Implications for the Crustal Growth of the Central Asian Orogenic Belt. *Petrology* **2020**, *28*, 403–417. [[CrossRef](#)]
51. Chen, F.; Hegner, E.; Todt, W. Zircon ages and Nd isotopic and chemical compositions of orthogneisses from the Black Forest, Germany: Evidence for a Cambrian magmatic arc. *Int. J. Earth Sci.* **2000**, *88*, 791–802. [[CrossRef](#)]
52. Chen, F.; Siebel, W.; Satir, M.; Terzioğlu, M.; Saka, K. Geochronology of the Karadere basement (NW Turkey) and implications for the geological evolution of the Istanbul zone. *Int. J. Earth Sci.* **2002**, *91*, 469–481. [[CrossRef](#)]
53. Goldstein, S.J.; Jacobsen, S.B. Nd and Sr isotopic systematics of river water suspended material: Implications for crustal evolution. *Earth Planet. Sci. Lett.* **1988**, *87*, 249–265. [[CrossRef](#)]
54. Jacobsen, S.B.; Wasserburg, G.J. Sm–Nd isotopic evolution of chondrites and achondrites, II. *Earth Planet. Sci. Lett.* **1984**, *67*, 137–150. [[CrossRef](#)]
55. Hoskin, P.W.O. Trace-element composition of hydrothermal zircon and the alteration of Hadean zircon from the Jack Hills, Australia. *Geochim. Cosmochim. Acta* **2005**, *69*, 637–648. [[CrossRef](#)]
56. Bell, E.A.; Boehnke, P.; Harrison, T.M. Recovering the primary geochemistry of Jack Hills zircons through quantitative estimates of chemical alteration. *Geochim. Cosmochim. Acta* **2016**, *191*, 187–202. [[CrossRef](#)]
57. Yan, W.; Casey, J.F. Synchronous formation of the ‘forearc’ Bay of Islands ophiolite and its basal high-temperature metamorphic sole constrained by U–Pb zircon ages. *Geosci. Front.* **2023**, *14*, 101649. [[CrossRef](#)]
58. Grimes, C.B.; Wooden, J.L.; Cheadle, M.J.; John, B.E. “Fingerprinting” tectono-magmatic provenance using trace elements in igneous zircon. *Contrib. Mineral. Petrol.* **2015**, *170*, 46. [[CrossRef](#)]
59. Middlemost, E.A.K. Naming materials in the magma/igneous rock system. *Earth-Sci. Rev.* **1994**, *37*, 215–224. [[CrossRef](#)]
60. Rickwood, P.C. Boundary lines within petrologic diagrams which use oxides of major and minor elements. *Lithos* **1989**, *22*, 247–263. [[CrossRef](#)]
61. Maniar, P.D.; Piccoli, P.M. Tectonic discrimination of granitoids. *GSA Bull.* **1989**, *101*, 635–643. [[CrossRef](#)]
62. Shimoda, G.; Tatsumi, Y.; Nohda, S.; Ishizaka, K.; Jahn, B.M. Setouchi high-Mg andesites revisited: Geochemical evidence for melting of subducting sediments. *Earth Planet. Sci. Lett.* **1998**, *160*, 479–492. [[CrossRef](#)]

63. Tatsumi, Y.; Shukuno, H.; Sato, K.; Shibata, T.; Yoshikawa, M. The Petrology and Geochemistry of High-Magnesium Andesites at the Western Tip of the Setouchi Volcanic Belt, SW Japan. *J. Petrol.* **2003**, *44*, 1561–1578. [[CrossRef](#)]
64. Tatsumi, Y.; Suzuki, T.; Kawabata, H.; Sato, K.; Miyazaki, T.; Chang, Q.; Takahashi, T.; Tani, K.; Shibata, T.; Yoshikawa, M. The Petrology and Geochemistry of Oto-Zan Composite Lava Flow on Shodo-Shima Island, SW Japan: Remelting of a Solidified High-Mg Andesite Magma. *J. Petrol.* **2006**, *47*, 595–629. [[CrossRef](#)]
65. Zheng, R.G.; Li, J.Y.; Xiao, W.J. Mid-Paleozoic ridge subduction in the Central Beishan of the southern Altaids: Evidence from geochemical, Sr-Nd and zircon U-Pb-Hf-O isotopic data of Gongpoquan volcanic rocks. *J. Geol. Soc.* **2019**, *176*, 755–770. [[CrossRef](#)]
66. Rapp, R.P.; Watson, E.B.; Miller, C.F. Partial melting of amphibolite/eclogite and the origin of Archean trondhjemites and tonalites. *Precambrian Res.* **1991**, *51*, 1–25. [[CrossRef](#)]
67. Rapp, R.P.; Watson, E.B. Dehydration Melting of Metabasalt at 8–32 kbar: Implications for Continental Growth and Crust-Mantle Recycling. *J. Petrol.* **1995**, *36*, 891–931. [[CrossRef](#)]
68. Rapp, R.P.; Shimizu, N.; Norman, M.D.; Applegate, G.S. Reaction between slab-derived melts and peridotite in the mantle wedge: Experimental constraints at 3.8 GPa. *Chem. Geol.* **1999**, *160*, 335–356. [[CrossRef](#)]
69. Sen, C.; Dunn, T. Dehydration melting of a basaltic composition amphibolite at 1.5 and 2.0 GPa: Implications for the origin of adakites. *Contrib. Mineral. Petrol.* **1994**, *117*, 394–409. [[CrossRef](#)]
70. Prouteau, G.; Scaillet, B.; Pichavant, M.; Maury, R.C. Fluid-present melting of ocean crust in subduction zones. *Geology* **1999**, *27*, 1111–1114. [[CrossRef](#)]
71. Sun, S.S.; McDonough, W.F. Chemical and isotopic systematics of oceanic basalts: Implications for mantle composition and processes. *Geol. Soc. Lond. Spec. Publ.* **1989**, *42*, 313–345. [[CrossRef](#)]
72. Xu, W.; Xu, X.Y.; Niu, Y.Z.; Chen, G.C.; Shi, J.Z.; Wei, J.S.; Song, B.; Zhang, Y.X. Geochronology, petrogenesis and tectonic implications of Early Permian A-type rhyolite from southern Beishan orogen, NW China. *Acta Petrol. Sin.* **2018**, *34*, 3011–3033. (In Chinese with English abstract)
73. Abdel-Karim, A.-A.M.; Azer, M.K.; Mogahed, M.M. Neoproterozoic concentric intrusive complex of gabbro-diorite-tonalite-granodiorite association, Rahaba area, southern Eastern Desert of Egypt: Implications for magma mixing of arc intrusive rocks. *Lithos* **2021**, *404–405*, 106423. [[CrossRef](#)]
74. Jung, S.; Hoernes, S.; Mezger, K. Synorogenic melting of mafic lower crust: Constraints from geochronology, petrology and Sr, Nd, Pb and O isotope geochemistry of quartz diorites (Damara orogen, Namibia). *Contrib. Mineral. Petrol.* **2002**, *143*, 551–566. [[CrossRef](#)]
75. France, L.; Koepke, J.; Ildefonse, B.; Cichy, S.; Deschamps, F. Hydrous partial melting in the sheeted dike complex at fast spreading ridges: Experimental and natural observations. *Contrib. Mineral. Petrol.* **2010**, *160*, 683–704. [[CrossRef](#)]
76. Yang, J.-H.; Wu, F.-Y.; Chung, S.-L.; Wilde, S.A.; Chu, M.-F. Multiple sources for the origin of granites: Geochemical and Nd/Sr isotopic evidence from the Gudaoling granite and its mafic enclaves, northeast China. *Geochim. Cosmochim. Acta* **2004**, *68*, 4469–4483. [[CrossRef](#)]
77. Wolf, M.B.; Wyllie, P.J. Dehydration-melting of amphibolite at 10 kbar: The effects of temperature and time. *Contrib. Mineral. Petrol.* **1994**, *115*, 369–383. [[CrossRef](#)]
78. Altherr, R.; Holl, A.; Hegner, E.; Langer, C.; Kreuzer, H. High-potassium, calc-alkaline I-type plutonism in the European Variscides: Northern Vosges (France) and northern Schwarzwald (Germany). *Lithos* **2000**, *50*, 51–73. [[CrossRef](#)]
79. Stern, C.R.; Kilian, R. Role of the subducted slab, mantle wedge and continental crust in the generation of adakites from the Andean Austral Volcanic Zone. *Contrib. Mineral. Petrol.* **1996**, *123*, 263–281. [[CrossRef](#)]
80. Eby, G.N. The A-type granitoids: A review of their occurrence and chemical characteristics and speculations on their petrogenesis. *Lithos* **1990**, *26*, 115–134. [[CrossRef](#)]
81. Chauvel, C.; Lewin, E.; Carpentier, M.; Arndt, N.T.; Marini, J.-C. Role of recycled oceanic basalt and sediment in generating the Hf–Nd mantle array. *Nat. Geosci.* **2008**, *1*, 64–67. [[CrossRef](#)]
82. Vervoort, J.D.; Plank, T.; Prytulak, J. The Hf–Nd isotopic composition of marine sediments. *Geochim. Cosmochim. Acta* **2011**, *75*, 5903–5926. [[CrossRef](#)]
83. Schmidt, M.W.; Jagoutz, O. The global systematics of primitive arc melts. *Geochem. Geophys. Geosyst.* **2017**, *18*, 2817–2854. [[CrossRef](#)]
84. Xu, W.; Zhu, D.-C.; Wang, Q.; Weinberg, R.F.; Wang, R.; Li, S.-M.; Zhang, L.-L.; Zhao, Z.-D. Constructing the Early Mesozoic Gangdese Crust in Southern Tibet by Hornblende-dominated Magmatic Differentiation. *J. Petrol.* **2019**, *60*, 515–552. [[CrossRef](#)]
85. Cornet, J.; Laurent, O.; Wotzlaw, J.F.; Antonelli, M.A.; Otamendi, J.; Bergantz, G.W.; Bachmann, O. Reworking subducted sediments in arc magmas and the isotopic diversity of the continental crust: The case of the Ordovician Famatinian crustal section, Argentina. *Earth Planet. Sci. Lett.* **2022**, *595*, 117706. [[CrossRef](#)]
86. Class, C.; Miller, D.M.; Goldstein, S.L.; Langmuir, C.H. Distinguishing melt and fluid subduction components in Umnak Volcanics, Aleutian Arc. *Geochem. Geophys. Geosyst.* **2000**, *1*, 1–28. [[CrossRef](#)]
87. Keller, C.B.; Schoene, B.; Barboni, M.; Samperton, K.M.; Husson, J.M. Volcanic–plutonic parity and the differentiation of the continental crust. *Nature* **2015**, *523*, 301–307. [[CrossRef](#)] [[PubMed](#)]
88. Schiano, P.; Monzier, M.; Eissen, J.P.; Martin, H.; Koga, K.T. Simple mixing as the major control of the evolution of volcanic suites in the Ecuadorian Andes. *Contrib. Mineral. Petrol.* **2010**, *160*, 297–312. [[CrossRef](#)]

89. Huang, H.; Niu, Y.; Mo, X. Garnet effect on Nd-Hf isotope decoupling: Evidence from the Jinfosi batholith, Northern Tibetan Plateau. *Lithos* **2017**, *274–275*, 31–38. [[CrossRef](#)]
90. Tang, M.; Wang, X.-L.; Shu, X.-J.; Wang, D.; Yang, T.; Gopon, P. Hafnium isotopic heterogeneity in zircons from granitic rocks: Geochemical evaluation and modeling of “zircon effect” in crustal anatexis. *Earth Planet. Sci. Lett.* **2014**, *389*, 188–199. [[CrossRef](#)]
91. Zhang, C.; Liu, D.; Zhang, X.; Spencer, C.; Tang, M.; Zeng, J.; Jiang, S.; Jolivet, M.; Kong, X.Y. Hafnium isotopic disequilibrium during sediment melting and assimilation. *Geochem. Perspect.* **2020**, *12*, 34–39. [[CrossRef](#)]
92. Chappell, B.W.; White, A.J.R. Two contrasting granite types: 25 years later. *Aust. J. Earth Sci.* **2001**, *48*, 489–499. [[CrossRef](#)]
93. Chappell, B.W.; White, A.J.R. I- and S-type granites in the Lachlan Fold Belt. *Earth Environ. Sci. Trans. R. Soc. Edinb.* **1992**, *83*, 1–26. [[CrossRef](#)]
94. King, P.L.; Chappell, B.W.; Allen, C.M.; White, A.J.R. Are A-type granites the high-temperature felsic granites? Evidence from fractionated granites of the Wangrah Suite. *Aust. J. Earth Sci.* **2001**, *48*, 501–514. [[CrossRef](#)]
95. Watson, E.B.; Wark, D.A.; Thomas, J.B. Crystallization thermometers for zircon and rutile. *Contrib. Mineral. Petrol.* **2006**, *151*, 413. [[CrossRef](#)]
96. Xu, W.; Weinberg, R.F.; Tian, S.-H.; Hou, Z.-Q.; Yang, Z.-S.; Chen, L.; Lai, F. K-Rich Adakite-Like Rocks in Central Tibet: Fractional Crystallization of a Hydrous, Alkaline Primitive Melt. *Geophys. Res. Lett.* **2023**, *50*, e2022GL099887. [[CrossRef](#)]
97. Roberts, M.P.; Clemens, J.D. Origin of high-potassium, calc-alkaline, I-type granitoids. *Geology* **1993**, *21*, 825–828. [[CrossRef](#)]
98. Karsli, O.; Dokuz, A.; Uysal, İ.; Aydin, F.; Chen, B.; Kandemir, R.; Wijbrans, J. Relative contributions of crust and mantle to generation of Campanian high-K calc-alkaline I-type granitoids in a subduction setting, with special reference to the Harşit Pluton, Eastern Turkey. *Contrib. Mineral. Petrol.* **2010**, *160*, 467–487. [[CrossRef](#)]
99. Yang, J.H.; Wu, F.Y.; Wilde, S.A.; Xie, L.W.; Yang, Y.H.; Liu, X.M. Tracing magma mixing in granite genesis: In situ U–Pb dating and Hf-isotope analysis of zircons. *Contrib. Mineral. Petrol.* **2007**, *153*, 177–190. [[CrossRef](#)]
100. Zhao, J.-L.; Zhang, X.; Wang, J.-R.; Tang, Q.-Y.; Zhou, W.-N.; Ma, X.-X. Syn-orogenic tectonomagmatic evolution of the Qilian Orogen: Insights from the Lumanshan gabbro–granite association in the Qilian Block, Northwest China. *Lithos* **2022**, *434–435*, 106922. [[CrossRef](#)]
101. Qin, K.Z.; Sakyi, P.; Tang, D.; Li, X.-H.; Sun, H.; Xiao, Q.-h.; Liu, P.-P. SIMS zircon U–Pb geochronology and Sr–Nd isotopes of Ni–Cu–Bearing Mafic–Ultramafic Intrusions in Eastern Tianshan and Beishan in correlation with flood basalts in Tarim Basin (NW China): Constraints on a ca. 280 Ma mantle plume. *Am. J. Sci.* **2011**, *311*, 237–260. [[CrossRef](#)]
102. Campbell, I.H.; Griffiths, R.W. Implications of mantle plume structure for the evolution of flood basalts. *Earth Planet. Sci. Lett.* **1990**, *99*, 79–93. [[CrossRef](#)]
103. Zheng, R.G.; Wu, T.R.; Zhang, W.; Meng, Q.P.; Zhang, Z.Y. Geochronology and geochemistry of late Paleozoic magmatic rocks in the Yinwaxia area, Beishan: Implications for rift magmatism in the southern Central Asian Orogenic Belt. *J. Asian Earth Sci.* **2014**, *91*, 39–55. [[CrossRef](#)]
104. Patiño Douce, A.E. Generation of metaluminous A-type granites by low-pressure melting of calc-alkaline granitoids. *Geology* **1997**, *25*, 743–746. [[CrossRef](#)]
105. Cawood, P.A.; Kröner, A.; Collins, W.J.; Kusky, T.M.; Mooney, W.D.; Windley, B.F.; Cawood, P.A.; Kröner, A. Accretionary orogens through Earth history. In *Earth Accretionary Systems in Space and Time*; Cawood, P.A., Kröner, A., Eds.; Geological Society of London: London, UK, 2009; Volume 318, pp. 1–36.
106. Zheng, R.G.; Li, J.Y.; Zhang, J. Juvenile hafnium isotopic compositions recording a late Carboniferous–Early Triassic retreating subduction in the southern Central Asian Orogenic Belt: A case study from the southern Alxa. *GSA Bull.* **2021**, *134*, 1375–1396. [[CrossRef](#)]
107. Li, J.; Wu, C.; Chen, X.; Zuzva, A.V.; Haproff, P.J.; Yin, A.; Shao, Z. Tectonic evolution of the Beishan orogen in central Asia: Subduction, accretion, and continent–continent collision during the closure of the Paleo-Asian Ocean. *GSA Bull.* **2022**, *135*, 819–851. [[CrossRef](#)]
108. Zuo, G.C.; Zhang, S.L.; He, G.Q.; Zhang, Y. Plate tectonic characteristics during the early Paleozoic in Beishan near the Sino-Mongolian border region, China. *Tectonophysics* **1991**, *188*, 385–392. [[CrossRef](#)]
109. Zuo, G.C.; Liu, C.Y.; Bai, W.C.; Feng, Y.Z. Volcano-Molasse Geological Structure and Geochemical Signature in Devonian Period Collision Orogenic in Beishan, Gansu-InMongolia. *Acta Geol. Gansu* **1995**, *4*, 35–43. (In Chinese with English abstract)
110. Du, J. Geochemical Characteristics and Tectonic Significance of the Jijitaizi Ophiolite in Beishan. Master’s Thesis, Lanzhou University, Lanzhou, China, 2019.
111. Cleven, N.; Lin, S.F.; Guilmette, C.; Xiao, W.J.; Davis, B. Petrogenesis and implications for tectonic setting of Cambrian suprasubduction-zone ophiolitic rocks in the central Beishan orogenic collage, Northwest China. *J. Asian Earth Sci.* **2014**, *113*, 369–390. [[CrossRef](#)]
112. Cleven, N.R.; Lin, S.F.; Xiao, W.J.; Davis, D.W.; Davis, B. Successive arc accretion in the southern Central Asian orogenic belt, NW China: Evidence from two Paleozoic arcs with offset magmatic periods. *Geol. Soc. Am. Bull.* **2018**, *130*, 537–557. [[CrossRef](#)]
113. Wang, X.Y.; Yuan, C.; Zhang, Y.Y.; Long, X.P.; Sun, M.; Wang, L.X.; Soldner, J.; Lin, Z.F. S-type granite from the Gongpoquan arc in the Beishan Orogenic Collage, southern Altai: Implications for the tectonic transition. *J. Asian Earth Sci.* **2018**, *153*, 206–222. [[CrossRef](#)]
114. Zhang, Y.; Yuan, C.; Sun, M.; Long, X.; Wang, Y.; Jiang, Y.; Lin, Z. Arc magmatism associated with steep subduction: Insights from trace element and Sr–Nd–Hf–B isotope systematics. *J. Geophys. Res. Solid Earth* **2017**, *122*, 1816–1834. [[CrossRef](#)]

115. Niu, W.C.; Xin, H.T.; Duan, L.F.; Wang, G.H.; Zhao, Z.L.; Zhang, G.Z.; Zheng, Y.L. The identification and subduction polarity of the Baiheshan ophiolite mélanges belt in the Beishan area, Inner Mongolia—New understanding based on the geological map of Qinghegou Sheet (1:50,000). *Geol. China* **2019**, *46*, 977–994. (In Chinese with English abstract)
116. Li, M.; Xin, H.T.; Ren, B.F.; Ren, Y.W.; Zhang, K.; Duan, X.L.; Niu, W.C.; Duan, L.F. Petrogenesis and Tectonic Significance of the Late Paleozoic Granitoids in Hazhu area, Inner Mongolia. *Earth Sci.* **2019**, *44*, 328–343. (In Chinese with English abstract)
117. Xin, H.T.; Niu, W.C.; Tian, J.; Teng, X.J.; Duan, X.L. Spatio-temporal structure of Beishan orogenic belt and evolution of Paleo-Asian Ocean, Inner Mongolia. *Geol. Bull. China* **2020**, *39*, 1297–1316. (In Chinese with English abstract)
118. Ding, J.; Han, C.; Xiao, W.; Wang, Z.; Song, D. Geochronology, geochemistry and Sr-Nd isotopes of the granitic rocks associated with tungsten deposits in Beishan district, NW China, Central Asian Orogenic Belt: Petrogenesis, metallogenic and tectonic implications. *Ore Geol. Rev.* **2017**, *89*, 441–462. [[CrossRef](#)]
119. Yuan, Y.; Zong, K.; Cawood, P.A.; Cheng, H.; Yu, Y.; Guo, J.; Liu, Y.; Hu, Z.; Zhang, W.; Li, M. Implication of Mesoproterozoic (~1.4 Ga) magmatism within microcontinents along the southern Central Asian Orogenic Belt. *Precambrian Res.* **2019**, *327*, 314–326. [[CrossRef](#)]
120. Zhang, W.; Pease, V.; Meng, Q.; Zheng, R.; Thomsen, T.B.; Wohlgemuth-Ueberwasser, C.; Wu, T. Timing, petrogenesis, and setting of granites from the southern Beishan late Palaeozoic granitic belt, Northwest China and implications for their tectonic evolution. *Int. Geol. Rev.* **2015**, *57*, 1975–1991. [[CrossRef](#)]
121. Zheng, R.; Li, J.; Xiao, W.; Zhang, J. Nature and provenance of the Beishan Complex, southernmost Central Asian Orogenic Belt. *Int. J. Earth Sci.* **2018**, *107*, 729–755. [[CrossRef](#)]
122. Zong, K.; Klemm, R.; Yuan, Y.; He, Z.; Guo, J.; Shi, X.; Liu, Y.; Hu, Z.; Zhang, Z. The assembly of Rodinia: The correlation of early Neoproterozoic (ca. 900 Ma) high-grade metamorphism and continental arc formation in the southern Beishan Orogen, southern Central Asian Orogenic Belt (CAOB). *Precambrian Res.* **2017**, *290*, 32–48. [[CrossRef](#)]
123. Ding, J.; Han, C.M.; Xiao, W.J.; Wang, Z.M.; Yang, X.M. Geochemistry and U-Pb geochronology of tungsten deposit of Huaniushan island arc in the Beishan Orogenic Belt, and its geodynamic background. *Acta Petrol. Sin.* **2015**, *31*, 594–616. (In Chinese with English abstract)
124. Feng, J.; Zhang, W.; Wu, T.; Zheng, R.; Luo, H.; He, Y. Geochronology and geochemistry of granite pluton in the north of Qiaowan, Beishan Mountain, Gansu province, China, and its geological significance. *Acta Sci. Nat. Univ. Pekin.* **2012**, *48*, 61–70. (In Chinese with English abstract)
125. Gao, F.; Jian, K.; Li, N.; Du, B.; Zhao, D.; Yi, P. U-Zircon U-Pb dating and geochemistry of Jijiquan pluton in the eastern section of Beishan orogenic belt and their tectonic implications. *Northwestern Geol.* **2018**, *51*, 26–37. (In Chinese with English abstract)
126. Gao, F.; Jian, K.K.; He, Y.F.; Li, N.; Yi, P.F.; Liu, X.W.; Tang, L. Genesis and metallogenic epoch constraints of Luzuizi antimony deposit of Beishan, Inner Mongolia. *Miner. Explor.* **2018**, *9*, 1644–1654. (In Chinese with English abstract)
127. He, Z.Y.; Zong, K.Q.; Jiang, H.Y.; Xiang, H.; Zhang, Z.M. Early Paleozoic tectonic evolution of the southern Beishan orogenic collage: Insights from the granitoids. *Acta Petrol. Sin.* **2014**, *30*, 2324–2338. (In Chinese with English abstract)
128. He, Z.Y.; Sun, L.X.; Mao, L.J.; Zong, K.Q.; Zhang, Z.M. Zircon U-Pb and Hf isotopic study of gneiss and granodiorite from the southern Beishan orogenic collage: Mesoproterozoic magmatism and crustal growth. *Chin. Sci. Bull.* **2015**, *60*, 389–399. (In Chinese with English abstract)
129. Liang, G.B.; Ding, S.P.; Li, Z.C.; Li, R.B.; Wang, M.; Chen, Y.X.; Pei, X.Z. Geochronology and geochemistry of Early Devonian-Late Silurian mylonitized quartz diorites from the southern Xiaoxigong in the Beishan area of Gansu Province and their geologic implications. *Northwestern Geol.* **2017**, *50*, 249–260. (In Chinese with English abstract)
130. Niu, Y.Z.; Lu, J.C.; Liu, C.Y.; Xu, W.; Shi, J.Z.; Song, B. Geochronology and distribution of the Upper Carboniferous-Lower Permian Ganquan Formation in the Beishan Region, northwestern China and its tectonic implication. *Geol. Rev.* **2018**, *64*, 1131–1148. (In Chinese with English abstract)
131. Niu, Y.Z.; Lu, J.C.; Liu, C.Y.; Song, B.; Shi, J.Z.; Xu, W. Chronostratigraphy and regional comparison of marine Permian System in the Beishan Region, North China. *Acta Geol. Sin.* **2018**, *92*, 1131–1148. (In Chinese with English abstract)
132. Tian, Y.; Li, J.; Ban, C.Y.; Yang, J.Y.; Zhou, J. Petrogeochemistry of Late Permian calc-alkaline intrusive rocks in Tamusu area of Alxa and its significances. *China Min. Mag.* **2020**, *29*, 251–255. (In Chinese with English abstract)
133. Wang, H. Meso-Neoproterozoic Magmatic-Metamorphic Events and Their Geological Significance in Southern Beishan Orogenic Belt. Master's Thesis, Chinese Academy of Geological Sciences, Beijing, China, 2022; 175p.
134. Xu, W. The Late Paleozoic Tectonic Framework and Evolution in Southern Beishan: Constraints from Paleomagnetism and Magmatism. Ph.D. Thesis, Chang'an University, Xi'an, China, 2019; 323p.
135. Yang, Z.X.; Ding, S.H.; Zhang, J.; Fan, X.X.; Kong, W.Q.; Zhao, J.C.; Jing, D.L. The discovery of Early Devonian adakites in Beishan orogenic belt and its geological significance. *Acta Petrol. Mineral.* **2021**, *40*, 185–201. (In Chinese with English abstract)
136. Yang, Z.X.; Zhao, J.C.; Jin, D.L.; Zhao, Q.H.; Zhang, J.; Fan, X.X. Chronological and Geochemical Characteristics of the Porphyritic Granodiorite in the Qianhongquan Area, Beishan Region, Gansu Province, China and Their Tectonic Significance. *Bull. Mineral. Petrol. Geochem.* **2021**, *40*, 228–241. (In Chinese with English abstract) [[CrossRef](#)]
137. Yang, Z.X.; Zhao, Q.H.; Zhang, J.; Chen, S.M.; Zhang, L.T.; Li, S.Y.; Jin, D.L.; Gong, Z.Z.; Zhao, J.C. Chronological and Geochemical Characteristics of the Heishantou Quartz-monzodiorite in the Beishan Area, Gansu Province, China, and Their Geological Significances. *Acta Metall. Sin.* **2022**, *41*, 1165–1177. (In Chinese with English abstract) [[CrossRef](#)]

138. Yi, P.F.; Li, N.; Gao, F.; Feng, W.H.; Tang, L.; Gao, Y.P.; Li, Q.; Liu, W.; Song, D.Y. LA-ICP-MS zircon U-Pb ages of the granites from Mashan of Inner Mongolia and their geological significances. *Geol. Bull. China* **2017**, *36*, 331–341. (In Chinese with English abstract)
139. Zhang, W.; Wu, T.R.; He, Y.K.; Feng, J.C.; Zheng, R.G. LA-ICP-MS zircon U-Pb ages of Xijianquanzi alkali-rich potassium-high granites in Beishan, Gansu Province, and their tectonic significance. *Acta Petrol. Mineral.* **2010**, *29*, 719–731. (In Chinese with English abstract)
140. Zhu, J.; Lv, X.B.; Peng, S.G.; Gong, Y.J.; Qiu, X.F.; Xiao, G.L. LA-ICP-MS zircon U-Pb geochronology and geochemical characteristics of the quartz syenite porphyry in the Xiaoxigong gold deposit and their geological implications. *Geol. Bull. China* **2015**, *34*, 1460–1469. (in Chinese with English abstract)

Disclaimer/Publisher’s Note: The statements, opinions and data contained in all publications are solely those of the individual author(s) and contributor(s) and not of MDPI and/or the editor(s). MDPI and/or the editor(s) disclaim responsibility for any injury to people or property resulting from any ideas, methods, instructions or products referred to in the content.